THE JOURNAL OF PHYSICAL CHEMISTRY B
A JOURNAL OF THE AMERICAN CHEMICAL SOCIETY

pubs.acs.org/JPCB
Article

Electrostatic Engineering of Phosphoketolase Enhances Activity on Small Nonphosphorylated Sugars and Improves Cell-Free ATP Regeneration from Inexpensive C_2-Substrates

Franziska Kraußer, Christopher M. Topham, Kenny Rabe, Jan-Ole Kundoch, Daniel Ohde, Andreas Liese, and Thomas Walther*

Cite This: J. Phys. Chem. B 2026, 130, 7791−7808
Read Online

ACCESS | Metrics & More | Article Recommendations | Supporting Information

ABSTRACT: Phosphoketolases can convert nonphosphorylated sugars to the high-energy compound acetyl phosphate and the versatile metabolic precursor acetyl-CoA. However, their application is limited by low catalytic activity toward these substrates. Here, we report the rational engineering of the phosphoketolase from *Bifidobacterium adolescentis* (Bad.F6Pkt) to enhance its activity and affinity toward glycolaldehyde (GA) and D-erythrulose (ERU) through reorganization of the protein electric field. Guided by predicted induced side-chain pK_a shifts, visualization of electrostatic potential difference maps alongside molecular modeling and sequence variation analyses, we identified mutations that could promote *in situ* ring opening of the predominant cyclic GA dimer. This approach yielded the GA-specific double mutant H142N:E153D, exhibiting a 10-fold improved affinity (K_M = 4.4 mM) and slightly enhanced catalytic efficiency compared to the previously reported H142N variant. In addition, the H256Y:H260Y:H548Y variant comprising long-range electrostatic mutations exhibited a 3.8-fold higher catalytic efficiency toward ERU than the wild-type. The engineered enzymes were evaluated in cell-free enzyme cascades for ATP regeneration via acetyl phosphate formation. The H142N variant enabled efficient ATP regeneration from GA and ethylene glycol, whereas H142N:E153D exhibited reduced stability under synthesis conditions. Furthermore, coupling of a D-threose aldolase and isomerase with the PKT triple mutant enabled rapid GA conversion to C_4 sugar intermediates, increasing the ATP yield.

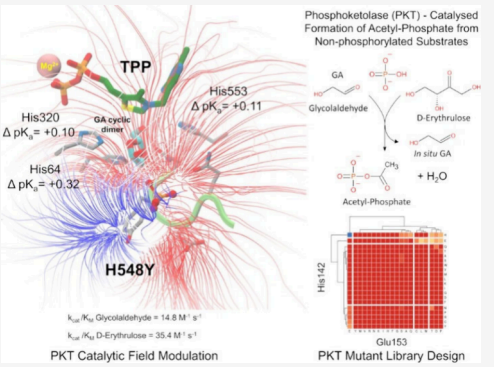

INTRODUCTION

The physiological function of phosphoketolases (PKTs) is to cleave the phosphorylated sugars D-xylulose 5-phosphate (X5P) or D-fructose 6-phosphate (F6P) into acetyl phosphate (acetyl-P) and D-glyceraldehyde 3-phosphate or D-erythrose 4-phosphate, respectively. X5P-specific PKTs are implicated in a xylose-degrading phosphoketolase pathway which is found in heterofermentative lactic acid bacteria. PKTs with activity on F6P facilitate degradation of hexoses in *Bifidobacteria* through the so-called 'bifid shunt'.[1−4] Acetyl-P can be readily converted to the metabolic hub molecule acetyl-CoA by the action of phosphate acetyltransferase (Pta).[5] Phosphoketolases have consequently attracted considerable attention in metabolic engineering endeavors to implement synthetic metabolic pathways for the carbon-conserving production of acetyl-CoA.[6−8]

Extending this concept, it has been recently shown that PKT enzymes are able to act on nonphosphorylated sugars, such as fructose, erythrulose, and glycolaldehyde.[6,7,9] This opens up the highly attractive prospect of applications that produce acetyl-P and downstream acetyl-CoA without the need to activate these sugars in ATP-consuming reactions. For instance, Lu et al.[7] have used PKTs to convert glycolaldehyde to acetyl-P. This enzyme-catalyzed reaction is a crucial step in the implementation of linear synthetic pathways that convert methanol into acetyl-CoA without carbon loss.[10] Kraußer et al. have reported that enzymatic cascades can be designed that chain substrate specific PKT activities on D-fructose, D-erythrulose (ERU), and glycolaldehyde (GA) to produce three mol of acetyl-P from one mol of fructose.[9] The high energy metabolite acetyl-P can be subsequently used to produce ATP via the acetate kinase reaction, thus, providing a convenient means to regenerate ATP from inexpensive sugars in cell-free reaction systems.[11]

Although PKT applications that exploit nonphosphorylated substrates are of considerable commercial interest in biotechnology, cognate PKTs unfortunately have inherently poor catalytic activities on non-natural substrates. Recent

Received: March 30, 2026
Revised: June 20, 2026
Accepted: July 7, 2026
Published: July 28, 2026

enzyme engineering studies[6,7,9] using the template PKT enzyme from *Bifidobacterium adolescentis* (Bad.F6Pkt), which has high cognate substrate activity and can be produced at comparatively high levels in *Escherichia coli*,[9] have focused on improving catalytic performance toward nonphosphorylated ketose sugars and GA. We have obtained significant improvements in D-fructose, ERU, and GA activity by single-mutation library screening at Bad.F6Pkt residue positions contacting a modeled bound open-chain covalent adduct reaction intermediate formed between the thiamine phosphate (TPP) cofactor and fructose-6-phosphate (F6P).[9] Nevertheless, a growing body of evidence concerning the nonadditive effects of single mutations on phosphoketolase[6,9] and closely related transketolase[12] activities on nonphosphorylated substrates strongly suggests that this type of epistasis is primarily electrostatic in origin. The coupling of the protein electric field to an enzyme reaction is widely believed to play a determinant role in catalysis.[13−15] Combinatorially antagonistic mutation-induced perturbations of the protein electric field are thus likely to account for difficulties in recovering native-like PKT catalytic activities on nonphosphorylated substrates. Physics-based modeling methods originally developed for studying enzyme-catalyzed reactions are increasingly being adapted to the diverse goals of computational enzyme design.[16−20] Improvements in enzyme variant catalytic properties through computational optimization of local electric fields underpin recasting of protein sequence space exploration as the electrostatic inverse folding problem.[13,21−24]

In the present study we aimed at further improvement in the catalytic activity of Bad.F6Pkt on GA since the aldehyde when present at elevated concentrations is known to inactivate phosphoketolases[10] and other enzyme systems[25,26] in addition to being toxic to cells.[27] Lysine ε-amino and arginine guanidinium side-chain groups are the principal targets in proteins of nonenzymatic glycation by GA and other highly reactive carbonyl species such as glyoxal or methylglyoxal.[28−30] Cross-linking of the minimum functional PKT dimer unit or the stable clover-leaf like tetramer of PKT dimers by GA could lead to unstable structural assemblies, while partially solvent-exposed lysine 605 and arginine 442 residues situated in the substrate binding channel of Bad.F6Pkt are vulnerable to chemical modification. In parallel, we sought PKT catalytic efficiency improvements toward the C_4 ketose ERU as GA can be conveniently converted to this sugar by chaining threose aldolase and threose isomerase reactions, thereby providing a means of maintaining low ambient GA concentration in the synthetic reaction pathway.

We have applied physics-based modeling techniques in conjunction with PKT family sequence variational analysis to fine-tune the catalytic field in Bad.F6Pkt and induce side-chain pK_a shifts in key histidine base catalytic residues. These modifications are proposed to compensate for the absence of substrate terminal phosphate groups by improving electrostatic preorganization in the Bad.F6Pkt active site.

The newly constructed enzymes were employed in a cell-free reaction system to regenerate ATP from inexpensive ethylene glycol (EG) by chaining EG dehydrogenase, GA-dependent PKT, and acetate kinase reactions (Figure 1). Additionally, we implemented a pathway to convert GA to ERU by coupling a highly GA-specific D-threose aldolase enzyme (*E. coli* fructose 6-phosphate aldolase variant Ec.FsaA L107Y:A129G[31]) with a D-threose isomerase (Figure 1).

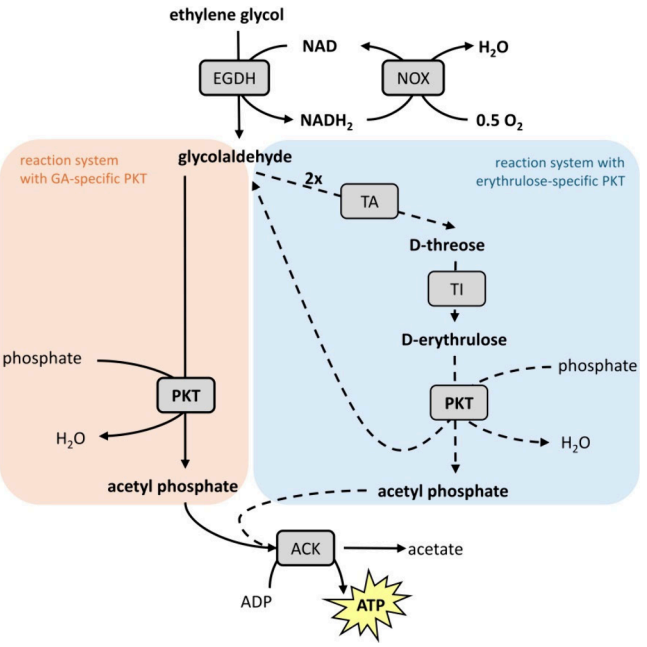

Figure 1. Enzymatic cascades for adenosine triphosphate (ATP) regeneration from ethylene glycol. Abbreviations: EGDH − ethylene glycol dehydrogenase, NOX − NADH oxidase, GA − glycolaldehyde, TA − threose aldolase, TI − threose isomerase, PKT − phosphoketolase, ACK − acetate kinase.

METHODS

Reagents and Chemicals

Unless otherwise stated, all chemicals were purchased from Merck KGaA (Darmstadt, Germany). Commercial kits for plasmid DNA isolation, gel DNA extraction, and PCR cleanup were obtained from New England Biolabs (Frankfurt am Main, Germany) and used according to the manufacturer's instructions. Synthetic genes were purchased from BioCat GmbH (Heidelberg, Germany) or Thermo Fisher Scientific Inc. (Waltham, MA, USA), while genomic DNAs were obtained from the German Collection of Microorganisms and Cell Cultures GmbH (DSMZ, Braunschweig, Germany). Genewiz Germany GmbH (Leipzig, Germany) or Eurofins Genomics (Ebersberg, Germany) carried out DNA sanger sequencing.

Plasmid Construction and Site-Directed Mutagenesis of *Bad.f6Pkt*

Plasmids used in this study to express the N-terminally 6x-His-tagged target genes are listed in Table S5. Mutations were introduced individually to the *Bad.f6pkt* gene by single site-directed mutagenesis using the PCR-based method described by Zheng and colleagues.[32] The PCR reaction was performed with Phusion High-Fidelity DNA polymerase (NEB), 62.5 ng of template vector, and primers listed in Supporting Information 2. After digestion of residual template DNA by DpnI restriction endonuclease (NEB), plasmids were transformed into chemically competent *E. coli* NEB 5-alpha cells (NEB). DNA sanger sequencing was used to verify respective mutations.

Protein Production

Expression of N-terminally 6x-His-tagged enzymes was carried out in *E. coli* strains harboring the corresponding pET-28a(+) expression vector. Gs.AckA and Ec.FsaA L107Y:A129G were

https://doi.org/10.1021/acs.jpcb.6c02050
J. Phys. Chem. B 2026, 130, 7791−7808

produced in *E. coli* BL21 (DE3) cells (New England Biolabs), whereas *E. coli* Rosetta(DE3) plysS (Merck KGaA) served as the host strain for all other enzymes, including Go.Gox0313 and Ms.Nox. The expression procedure was based on the method described previously.[8,9] Briefly, cultures were grown in LB medium at 37 °C to mid log phase, induced with 1 mM isopropyl-β-D-thiogalactopyranoside (IPTG), and incubated at 25 °C for 20 h. Production of Bad.F6Pkt and Ms.Nox was carried out using the autoinducing medium ZYM-5052,[33] which was inoculated with an initial optical density at 600 nm of 0.05, prior to incubation at 25 °C for 24 h.

Protein Purification, Quantification, and Storage

Protein purification was performed following the procedure described previously.[9] Briefly, cell-free crude extract was applied to 0.35 mL of Talon Cobalt affinity resin (Cytiva, Marlborough, USA) and incubated at room temperature with rotation at 20 rpm (RevolverTM, Labnet, Edison, NJ, USA) for 1 h. The resin was washed twice with buffer (10 mM KH_2PO_4, 300 mM NaCl, pH 7.5) before bound His-tagged enzymes were eluted using 0.5 mL of elution buffer (10 mM KH_2PO_4, 300 mM NaCl, 500 mM imidazole, pH 7.0). Buffer exchange of the eluate was performed with an Amicon Ultra-0.5 centrifugal filter unit (pore size 10 kDa; Merck Millipore, USA). By centrifugation (1000 g, 4 °C, 2 min.) the protein fraction was recovered in 0.4 mL of storage buffer (10 mM KH_2PO_4, 300 mM NaCl, pH 7.0) and stored at 4 °C until further use. Purified Ms.Nox solution was supplemented with 1 mM flavin adenine dinucleotide (FAD) prior to storage. Protein concentrations were determined by the Bradford assay (Roti-Quant, Carl Roth, Karlsruhe, Germany) using bovine serum albumin (0−100 μg mL^{-1}) as the calibration standard.

Multiple Sequence Alignment Residue and Residue-Pair Amino Acid Frequency Analyses

Position-dependent residue type frequencies and relative Shannon information entropy measures of residue variability (H_X) in an HMM multiple sequence alignment (MSA) comprising 1019 PKT enzyme family sequences[9] were calculated using SEQUESTER[34] from sequence-weighted data counts to reduce phylogenetic bias. MSA sequence weights were calculated according to the method of Morcos et al.[35] for $q = 20$ native amino acid residue types with an identity cutoff of 80%, before normalization to sum to the total number of sequences. H_X values at position X in the Bad.F6Pkt sequence fall within the limits of zero, corresponding to a fully conserved residue position, and one, for a position showing no intrinsic residue type preference.

Sequence weighted frequency counting was also applied in the calculation of statistical correlation energy measures, $-\ln g(X_i,Y_j)$, of the pairwise dependence of residue type (i = 1,20) at position X on the residue type (j = 1,20) at position Y in the MSA. The correlation $g(X_i,Y_j)$ is given by $\frac{p_{(i,j|X,Y)}}{p_{(i)}p_{(j)}}$, where $p_{(i,j|X,Y)}$ is the conditional pairwise probability of observing (i,j) residue types respectively at positions X and Y. Background probabilities of residue type occurrence $(p_{(i)},p_{(j)})$ were taken as mean frequency values for all proteins.[36] Data frequency seeding was implemented to address dual concerns of data sparseness and rare or forbidden events. Seed counts were set as $q^2\, p_{(i)}\, p_{(j)}$, corresponding to an average of a single phantom count per residue type combination. Favorable or most frequently observed residue type combinations at a given pair of residue positions are associated with negative values of $-\ln g(X_i,Y_j)$, whereas positive values of the statistical energy measure correspond to unfavorable or infrequently observed combinations. A zero score implies the lack of dependence between the two residue types.

Molecular Modelling of Bad.F6Pkt-TPP Complex with Glycolaldehyde Cyclic Dimer

The close structural resemblance of the five-membered 2-hydroxymethyl-4-hydroxy-1,3-dioxalane (Figure S1) and the β-furanose ring form of D-fructose was exploited to construct a model of the glycolaldehyde cyclic dimer bound to the Bad.F6Pkt-TPP complex. Docking of a HF/6−31G* geometry-optimized 2-hydroxymethyl-4-hydroxy-1,3-dioxalane ligand molecule was carried out by superposition of the C2, O1, C5, C4, and O3 atom centers on the structurally equivalent C2, C3, C4, C5, and O5 β-furanose ring skeleton atoms in the previously described modeled complex of D-fructose with Bad.F6Pkt and Mg-TPP.[9] Following excision of the D-fructose ligand coordinates, the resultant structure was then energy minimized in the presence of nonoverlapping X-ray crystallographic water molecules abstracted from the *Bifidobacterium breve* Pkt H320A mutant homologue template (PDB code 3ahi) used in the modeling of Bad.F6Pkt.[9] The *ff99SB* Amber molecular mechanics force field[37] was used for protein atoms, and the electrostatic model comprised a distance-dependent dielectric constant with $\varepsilon = 4$. GAFF force field parameters[38] and partial charges for the 4′-aminopyrimidine tautomeric form of TPP^{2-}[39] were as previously reported.[9] A complete list of GAFF atom types and RESP[40] partial charges for 2-hydroxymethyl-4-hydroxy-1,3-dioxalane is provided in Table S1 of the Supporting Information. All Hartree−Fock (HF) quantum chemical calculations were performed using GAMESS.[41]

Protein Continuum Electrostatics Calculations

Ionizable (Asp, Glu, His, Lys, and Arg) protein residue pK_a calculations were performed on wild type Bad.F6Pkt and minimally disturbed mutant enzyme model coordinate sets using DelPhiPKa version 2.3.[42,43] Parameters for the reference dielectric constant (ε) in the Gaussian distribution formula for the protein interior and the variance (σ) of the Gaussian distribution were left at their respective default values of 8.0 and 0.70. A 12 Å cluster threshold delimitation was used. The C++ software code for automated hydrogen atom placement was modified before compilation of the program to permit adjustment of protein mainchain secondary amide N−H bond lengths from 1.5 Å to 1.0 Å. The default AMBER force-field was used in all calculations. Reference side-chain pK_a values for L-glutamic acid (4.00) and L-histidine (6.50) in water were respectively altered in the steering data input file to 4.31[44] and 6.20[45] in closer agreement with experimental values. Simulated residue titrations in the pH range 0 to 14 were carried out at pH intervals of 0.5.

Side-chain mutations were initially introduced into the dimeric wild type Bad.F6Pkt enzyme model using the COOT interactive molecular graphics and modeling package[46] before the application of a single round of energy minimization. Any significant conformational changes to the protein residue side-chain geometry arising from energy minimization were reintroduced into the starting atomic coordinate set. A single Mg-TPP cofactor microstate was included in all Poisson−Boltzmann continuum electrostatic calculations. Atomic charges for the TPP^{2-} 4′-aminopyrimidine tautomer were taken from Lie et al.,[39] and the corresponding radii were taken

https://doi.org/10.1021/acs.jpcb.6c02050
J. Phys. Chem. B 2026, 130, 7791−7808

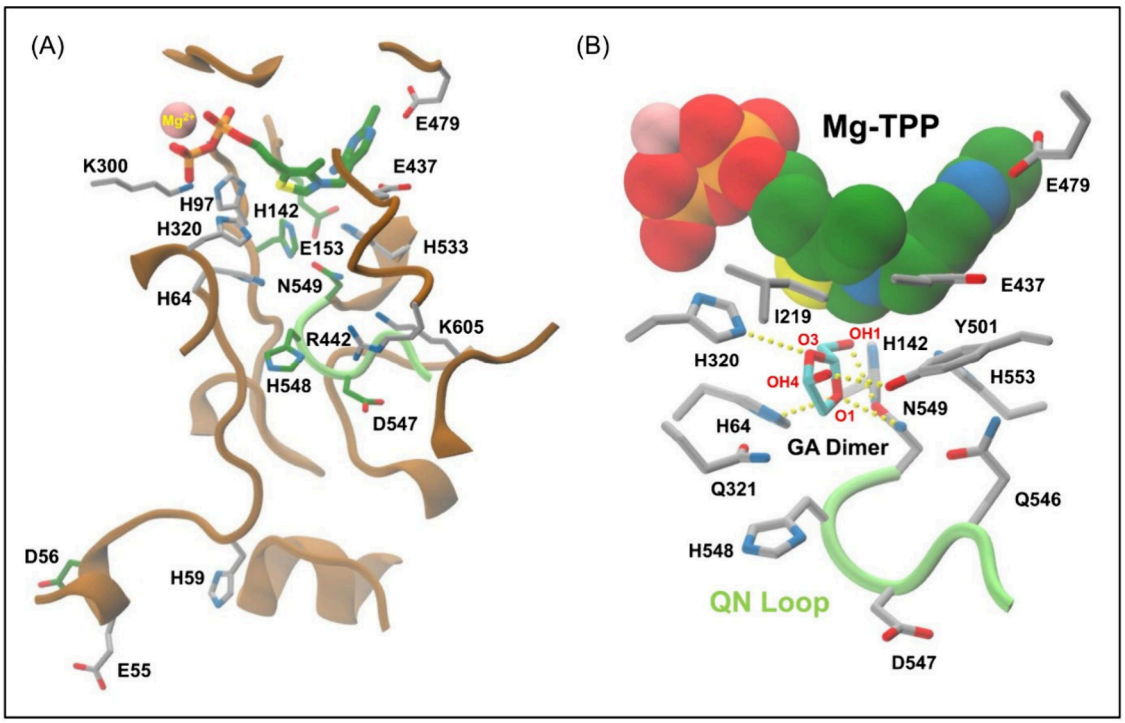

Figure 2. Substrate binding channel in Bad.F6Pkt. **(A)** The TPP stick representation is colored according to element type: carbon, green; nitrogen, blue; oxygen, red; sulfur, yellow; phosphorus, orange. The bound Mg^{2+} ion is shown as a pink colored van der Waals sphere. Side-chain carbon atoms at mutated enzyme residue positions are colored in green and in gray at ionizable residue positions used to monitor shifts in calculated pK_a values arising from mutation (see Methods). **(B)** The Mg-TPP cofactor is shown as van der Waals spheres using the same color scheme. Bad.F6Pkt residue side-chain (gray carbons) good quality hydrogen bonding interactions with the cyclic GA dimer, 2-hydroxymethyl-4-hydroxy-1,3-dioxalane (Supporting Information Figure S1) depicted with cyan colored carbon atoms, are indicated by yellow solid sphere vectors.

from the standard Bondi compendium[47] with minor adjustments.

Poisson−Boltzmann electrostatic potential ($\varphi(\mathbf{r})$) grid calculations on PQR-formatted coordinate sets generated by DelPhiPKa comprising prevalent protein residue ionization states at pH 7 were performed using APBS version 3.4.1[48] with an internal dielectric constant (ε) of 4 and at an ionic strength of 0.15 M. DX-formatted $\Delta\varphi(\mathbf{r})$ electrostatic potential difference volumetric maps, calculated by subtraction of mutant and wild-type enzyme electrostatic potential ($\varphi(\mathbf{r})$) grids using the *dxmath* APBS conversion utility, were displayed as isopotential surfaces and field lines in the VMD graphics program.[49]

Enzymatic Assays

An Infinite M200 PRO plate reader (Tecan AG, Switzerland), I-control software (version 3.8.2.0, Tecan AG), and 96-well flat-bottomed microplates (Thermo Fisher Scientific Inc.) were used to determine the activities of purified enzymes. One unit of enzyme activity (U) is defined as the synthesis of 1 micro mole of product per minute. Experimental data were fitted to the Michaelis−Menten or substrate inhibition model using the Curve Fitting Tool in MATLAB (version R2023b, MathWorks Inc., Natick, MA, USA) to determine the enzyme's Michaelis constant (K_M) and maximum reaction velocity (V_{max}).

Enzymatic activity of phosphoketolase was determined as described previously[9] using the hydroxamate assay[50,51] to detect the product acetyl-P. The enzymatic reaction was carried out at 37 °C and pH 6.5 in the presence of 50 mM KH_2PO_4, 3.8 mM $MgCl_2$, and 0.8 mM TPP using either 200 mM GA or 25 mM ERU as the substrate. For the estimation of kinetic parameters, specific activity was measured at substrate concentrations ranging from 0−300 mM (GA) or 0−100 mM (ERU).

D-Threose isomerase activity was quantified by the detection of ERU using D-erythrulose reductase from *Gallus gallus* (Gg.DER) in a coupled assay adapted from the procedure described by Morii et al.[52] The reductase enzyme was expressed, purified, and stored as described previously.[9] The reaction mixture with a total volume of 250 μL contained 100 mM HEPES buffer pH 7.0, 1 mM $MnCl_2$, 0.2 mM NADH (dissolved in 10 mM NaOH), 8 μg mL^{-1} Gg.DER and appropriate quantities of the purified isomerase enzyme. The enzymatic reaction was initiated by addition of D-threose in concentrations ranging from 0−80 mM and monitored continuously at 37 °C by the detection of NADH at 340 nm.

The activity of ethylene glycol dehydrogenase in the oxidative direction was determined by monitoring the reduction of NAD^+ at 340 nm and 37 °C. The reaction mixture contained 100 mM HEPES buffer pH 7.0, 0.5 mM NAD^+, and appropriate amounts of purified enzyme. Reactions were started by the addition of ethylene glycol at variable concentrations (0−100 mM).

NADH oxidase activity was quantified by monitoring the consumption of NADH at 340 nm and 37 °C. Appropriate quantities of the purified enzyme were present in 100 mM HEPES buffer pH 7.0, and the reaction was initiated by the addition of 0.25 mM NADH.

In Vitro sn-Glycerol 3-Phosphate (G3P) Synthesis

The reaction mixture for *in vitro* G3P synthesis contained 200 mM HEPES buffer (pH 7.0), 1 mM ATP, 0.8 mM TPP, 4 mM $MgCl_2$, 32 mM sodium phosphate (pH 7.0) and glycerol, 5 μg mL^{-1} Gs.AckA, and 0.3 mg mL^{-1} Cs.GlpK, unless otherwise

https://doi.org/10.1021/acs.jpcb.6c02050
J. Phys. Chem. B 2026, 130, 7791−7808

stated. The following enzymes were added as required: Bad.F6Pkt (variants), Go.Gox0313, Ms.Nox, Ec.FsaA L107Y:A129G, and Ps.LrhI. After a preliminary incubation at 37 °C for 5 min, the reactions was initiated by the addition of either 25 mM ERU, 15 or 25 mM GA, or 100 mM EG. Each reaction (1 mL total volume) was performed in a 2 mL tube and incubated at 37 °C for 26 h. Reactions containing EG as the substrate were supplemented with 2 mM NAD^+ and shaken at 220 rpm. Samples of 50 μL were obtained at regular intervals and subsequently diluted 1:4 in 0.1 M HCl to quench enzymatic activity, followed by immediate cooling on ice. For real-time, offline monitoring of G3P production using the coupled enzymatic assay described below, a portion of each quenched sample was further diluted in 0.1 M HEPES buffer (pH 7.5). The remaining aliquots were stored at −20 °C until further analysis.

Quantification of Substrates, Intermediates, and Products

The target product G3P was quantified using the photometric method described previously.[9] Briefly, G3P is converted by *sn*-glycerol 3-phosphate oxidase (G3Pox, Creative Enzymes, USA) to dihydroxyacetone phosphate and hydrogen peroxide. In the presence of 4-aminoantipyrine (4-AAP) and sodium 3,5-dichloro-2-hydroxybenzenesulfonate (DHBS), the subsequent peroxidase-catalyzed reaction consumes one mole of H_2O_2 to yield one mole of water and quinone imine, which is detected photometrically at 520 nm. Absorbance was monitored at 30 °C until signal stabilization and G3P concentration was determined from the absorbance difference between the sample and a control reaction lacking G3Pox.

Ethylene glycol, glycolaldehyde, C_4 sugars, glycolate, glycerol, and acetate were quantified by high-performance liquid chromatography (UltiMate3000, Thermo Fisher Scientific, USA) equipped with a DAD-detector (DAD-3000(RS), Thermo Fisher Scientific, USA), a RI-detector (RefractoMax 520, ERC, Germany), and an autosampler with a temperature set to 6 °C. After appropriate dilution in ddH_2O, samples were filtered (0.2 μm PTFE filter) before injection of 20 μL to the Rezex ROA-Organic Acid H^+ (8%) column (Phenomenex). Analytes were eluted with 0.5 mM H_2SO_4 at a flow rate of 0.5 mL min^{-1} and a temperature of 65 °C.

RESULTS

Optimisation of the Catalytic Field in Bad.F6Pkt to Promote Catalysis on Nonphosphorylated Substrates

The phosphoketolase (PKT) from *Bifidobacterium adolescentis* (Bad.F6Pkt) was used here as the template for enzyme engineering of enhanced binding and activity toward ERU and GA nonphosphorylated substrates. Bad.F6Pkt is a member of the XFPK (EC 4.1.2.22) phosphoketolase subfamily present in *Bifidobacterium* species operating a bifid-shunt fermentation pathway. XFPK enzymes display comparable specificities for cyclic fructose 6-phosphate (F6P) and acyclic xylulose 5-phosphate (X5P) substrates, while the common PKT form present in most organisms (XPK, EC 4.1.2.9) is mainly specific for X5P.[53] Previously we identified a Bad.F6Pkt variant (H548N) with 5.6-fold increased activity on the non-phosphorylated substrate D-fructose, a 2.2-fold increase in ERU activity, and a 1.3-fold increase in GA activity compared to the wild-type enzyme.[9] However, this mutation in the mobile QN (Q546-N549) loop[54,55] in the substrate binding channel (Figure 2A) did not lower K_M for ERU or GA (Table 2), although this is a prerequisite for the implementation of an *in vitro* reaction system that avoids GA accumulation to reduce enzyme inactivation (see Figure 1). The QN-loop exists as inconvertible open and closed conformational forms, illustrated in Figure S2. The open conformer is widely believed to permit access of the F6P and X5P substrates and facilitate release of the respective erythrose 4-phosphate and glyceraldehyde 3-phosphate first reaction products. The closed form ensures the proper positioning and catalytic processing of the donor substrate and substrate-TPP conjugate. Conformational fluctuation in the QN-loop appears to be almost entirely driven by pronounced main-chain dihedral angle shifts accompanied by Ramachandran plot regional zone[56] changes at the G550 and N549 residue positions (Figure S2B). The +ve φ main-chain conformation of G550 in the open conformation is notably unfavorable, and the presence of incompatible bulky residue types at this position in 28% of all PKTs (Figure S7) suggests that the QN-loop is effectively locked in the closed conformation in these enzymes.

The PKT reaction mechanism for the conversion of the cognate F6P and X5P substrates to acetyl-P is well established.[57−60] Scheme S1 illustrates key reaction intermediates and catalytic steps for the multiple-step formation of acetyl-P from the acylic four-carbon ERU ketose. Computational simulation of the PKT-catalyzed conversion of glycolaldehyde to acetyl-P[7] implicated the involvement of the reactive aldehyde group of the monomeric glycolaldehyde species and the participation of the protonated H553 residue tautomer in the formation of the α,β-dihydroxyethyl TPP (DHETPP) enzyme reaction intermediate.[57,60] The alternative reaction pathway for PKT-catalyzed GA conversion is integrated in Scheme S1, revealing catalytic steps in common with the reaction of ERU. GA exists in the solid crystalline state as a six-membered cyclic dimer (2,5-dihydroxy-1,4-dioxane) which dissociates in aqueous solution via an acyclic intermediate to yield a recyclized dimer, identified as 2-hydroxymethyl-4-hydroxy-1,3-dioxolane (Figure S1), along with different monomeric forms.[61] Quantitative analysis indicates that GA is predominantly present in solution as a hydrated monomer (70−75%), with the five-membered 2-hydroxymethyl-4-hydroxy-1,3-dioxolane cyclic dimer accounting for approximately 17%. A mere 4−5% of GA exists in its monomeric form with a reactive aldehyde moiety.[62,63] The capacity of PKT to catalyze GA conversion would appear to be impaired by the low abundance of the reactive substrate species, acting as an effective brake on net flux through the synthetic reaction pathway for the generation of ATP.

Enzyme catalytic efficiency has been postulated by Warshel[64,65] to originate from the intramolecular protein electric field that permanently favors the reaction transition state (TS) over the reactants. Protein electrostatic preorganization not only provides favorable enthalpic contributions to TS binding but also permits enzyme-catalyzed reactions to avoid an entropic penalty associated with the reorganization of the environment during TS crossing. Vibrational Stark effect (VSE) spectroscopy has been used to experimentally demonstrate the correlation between enzyme catalytic rate enhancement and the magnitude of the electric field in the active site.[66] The k_{cat}/K_M enzyme specificity constant kinetic parameter corresponds to the rate constant for the reaction of free enzyme with substrate.[67] According to transition-state theory, k_{cat}/K_M can be related to the free energy difference between the rate-limiting enzyme-reaction TS energy barrier and the free enzyme state. This conveniently allows changes in

https://doi.org/10.1021/acs.jpcb.6c02050
J. Phys. Chem. B 2026, 130, 7791−7808

Table 1. Computed Residue pK_a Values in Bad.F6Pkt and Shifts Due to Substrate Terminal Phosphate Group Binding and Mutation[a]

Bad.F6Pkt Residue Position	RSA (%)	Wild Type	Wild Type + PO_4^{2-}[b]	H548N	H548Y	H260Y:H548Y	H256Y:H260Y: H548Y	H142N	H142N: E153D
D26	13	1.97	1.97	1.97	1.97	2.42 (+0.45)	2.76 (+0.79)	1.97	1.97
H59	26	5.55	5.63	5.63	5.63	5.64	5.63	5.58	5.58
H64	2	5.08	5.70 (+0.62)	5.28 (+0.20)	5.40 (+0.32)	5.42 (+0.34)	5.41 (+0.33)	5.42 (+0.34)	5.47 (+0.39)
H97	0	6.09	6.13	6.09	6.09	6.10	6.10	6.16	6.20 (+0.11)
H142	2	4.90	4.98	4.96	4.95	4.96	5.00 (+0.10)	NA	NA
E153	21	2.23	2.27	2.25	2.25	2.26	2.26	2.43 (+0.20)	1.81 (−0.43)
H256	46	6.08	6.08	6.08	6.08	6.21 (+0.13)	NA	6.08	6.08
H260	0	6.38	6.38	6.38	6.39	NA	NA	6.41	6.42
K300	0	11.86	12.02 (+0.16)	11.85	11.86	11.86	11.86	11.86	11.87
H320	2	4.64	5.18 (+0.54)	4.70	4.74 (+0.10)	4.75 (+0.11)	4.76 (+0.12)	4.66	4.67
E437	1	2.23	2.47 (+0.23)	2.28	2.28	2.28	2.28	2.30	2.30
R442	31	13.16	Undet.	13.15	13.14	13.15	13.15	13.17	13.16
E479	1	2.58	2.63	2.59	2.59	2.59	2.59	2.63	2.63
D547	26	1.19	1.64 (+0.45)	1.40 (+0.21)	1.40 (+0.21)	1.40 (+0.21)	1.40 (+0.21)	1.22	1.23
H548	29	5.52	6.51 (+0.99)	NA	NA	NA	NA	5.52	5.53
H553	0	4.93	5.38 (+0.45)	5.02	5.04 (+0.11)	5.04 (+0.11)	5.03 (+0.10)	5.14 (+0.21)	5.20 (+0.27)
K605	19	10.76	12.98 (+2.22)	10.80	10.80	10.80	10.80	10.77	10.76

[a]Calculations at ionizable residue positions were carried out on modelled wild-type and mutant Bad.F6Pkt complexes with Mg-TPP using DelPhiPKa as described in Methods. Tabulated predicted pK_a values at selected positions are averages over both chains in the dimeric enzyme. For clarity, only induced pK_a shifts relative to the wild type enzyme (ΔpK_a) of $\geq \pm 0.1$ in magnitude are indicated in parentheses. RSA, side-chain residue solvent accessible surface area relative to that in corresponding extended conformation Ala-XXX-Ala model reference tri-peptide structure.[72] NA, not applicable. [b]Surrogate PO_4^{2-} ion probe atomic coordinates were abstracted as the terminal phosphate group of the open-chain form of F6P in an overlaid copy of the modelled TPP-F6P (T6F) covalent adduct complex with Bad.F6Pkt.[9] Specific binding of the inorganic phosphate cosubstrate occurs at an independent site separated by the equivalent of four covalent bond lengths from the position of the ion probe, estimated to be approximately 5.3 Å as illustrated in Figure S2. Undet., could not be determined.

k_{cat}/K_M arising from mutation or other perturbation to be inferred from predicted modulation of the protein electric field in the free or unbound enzyme state.

Here we employ the Poisson−Boltzmann (PB) continuum electrostatics model as a computationally tractable framework for the calculation of ionizable protein residue pK_a values, electrostatic potential ($\varphi(\mathbf{r})$), and field strength[18,68−70] in mutant and wild type enzyme complexes with the Mg-TPP cofactor in the closed QN-loop conformational state. Although calculated mutant - wild-type difference electrostatic potential ($\Delta\varphi(\mathbf{r})$) grids cannot of course provide any direct information concerning mutant- and/or substrate-dependent rate-limiting reaction steps, this can sometimes be inferred in our rational approach to PKT redesign from experimentally determined kinetic parameter feedback obtained by probe mutation and induced shifts in predicted residue side-chain pK_a values. The PB-based model allows for electrostatic polarization to be taken into account of at all positions in the Bad.F6Pkt-TPP dimer. This is particularly advantageous in the fine-tuning of local electric fields as a means of improving catalysis toward nonphosphorylated substrates in mutant enzymes.

Bad:F6Pkt is an acidic protein with an isoelectric point (pI) of 4.2, determined by simulated titration (Figure S3) using DelPhiPKa.[42,43] The observed field line high density in the substrate binding channels of the dimeric enzyme is in direct proportion to the electric field strength (Figure S4). Of the five identifiable ionizable histidine residue positions in the wild-type active site (Figure 2), four (64, 97, 142, and 320) are fully buried with side-chain relative solvent accessibility (RSA) values below 7%. The imidazole side chain of H548 in the QN loop is partially buried, principally through interaction with the neighboring D547 acidic residue, with an RSA value (29%) in the range 7−40%. Calculated side-chain pK_a values of all the histidine residues in the active site apart from H97 are lower than experimentally determined macroscopic side-chain pK_a values of 6.02[71] and 6.20[45] for L-histidine in aqueous solution (see Table 1).

In situ ring-opening of cyclic substrates such as D-fructose and the GA dimer species is potentially rate-limiting in the PKT-catalyzed conversions of these nonphosphorylated substrates to acetyl-P. The β-furanose ring form of the cognate PKT substrate fructose 6-phosphate is believed to be linearized in the active site either by protonation of the ring oxygen (acid catalysis) or deprotonation of the anomeric C2 hydroxyl group (base catalysis), both of which have been suggested to be assisted by the 6-phosphate group via mediating solvent molecules.[60] Since 2-hydroxymethyl-4-hydroxy-1,3-dioxalane does not possess an anomeric hydroxyl group, ring opening of the GA cyclic dimer may be expected to occur by acid catalysis. An energy minimized model complex of wild type Bad.F6Pkt enzyme with Mg-TPP and the bound cyclic GA dimer is shown in Figure 2B. The C2 ring atom in the GA dimer is separated by approximately 4 Å from the C2 TPP thiazolium ring carbon with which a covalent adduct is formed in the first step of the cognate F6P substrate reaction mechanism.[57,60] The O1 ring oxygen is hydrogen bonded by the flanking N549 and H64 side-chains, while N549 can make an additional hydrogen bond with the 2-hydroxymethyl group. Substrate-specific interactions of the open chain TPP-F6P covalent adduct with the N549 residue in the *Bifidobacterium breve* (XFPK) enzyme were reported in recent docking simulation studies.[53] H320 and Y501 are respectively able to form hydrogen bonds with the GA-dimer O3 ring oxygen and the 4-hydroxyl group. H64 has been proposed as a putative proton acceptor in the deprotonation of the C3 hydroxyl in C3−C4 bond cleavage of the natural substrate F6P.[58,59] Acid-

https://doi.org/10.1021/acs.jpcb.6c02050
J. Phys. Chem. B 2026, 130, 7791−7808

catalyzed GA dimer ring opening could be mediated by a solvent proton or the direct participation of the protonated H64 side-chain tautomeric state.

The five-membered 2-hydroxymethyl-4-hydroxy-1,3-dioxalane GA cyclic dimer (Figure S1) notably bears a close structural resemblance to the β-furanose ring form of F6P, whereas D-fructose is sterically constrained to predominantly exist in the six-membered β-pyranose ring form.[73] The postulated involvement of the 6-phosphate group in F6P ring opening[60] prompted us to investigate the influence of a single bound PO_4^{2-} ion, extracted from a TPP-F6P model complex,[9] on the calculated side-chain pK_a values of ionizable residues lining the substrate binding channel (Table 1). The predicted pK_as of the catalytic reaction center H64, H320, and H553 residue side chains were respectively shifted upward by the presence of the phosphate ion by 0.62, 0.54, and 0.45 units. The calculated pK_a of the D547 residue side chain close to PO_4^{2-} ion binding site was also raised to a similar degree (0.45). The H64 and H320 residues have been variously inferred from substrate-adduct docking simulations to be the B_2 catalytic base (Scheme S1) in XFPK enzymes responsible for deprotonation of the F6P C3 hydroxyl group in the second (aldose phosphate product formation) reaction step,[60] whereas the H553 equivalent residue (H559) in the *Lactococcus lactis* XPK enzyme was assigned as the B_2 catalyst.[53] The B_2 catalyst is also involved in the following DHETPP dehydration step common to all substrate reaction mechanisms[60] as indicated in Scheme S1. It is noteworthy that in the docked and cross-docked simulated PKT enzyme−substrate complexes reported by Scheidig et al.,[53] the terminal phosphate group of the X5P-TPP covalent adduct was positioned closer to the three catalytic reaction center histidine residues with predicted perturbed pK_a values incurred by PO_4^{2-} ion binding, than was the 6-phosphate group of F6P-TPP.

Collectively these findings suggest that in addition to an established steric role in the preferential stabilization of the β-furanose ring form of the cognate F6P substrate, the 6-phosphate group not only may assist ring opening in F6P by raising the pK_a of H64 in the catalytic reaction center of XFPK enzymes but also may aid deprotonation of TPP-F6P adduct via modulation of the B_2 catalytic base pK_a. Electrostatic mutations in Bad.F6Pkt able to mimic the induced effects of the terminal phosphate groups in cognate substrates can thus be anticipated to promote ring opening of the prevalent GA-dimer form in solution, with concomitant *in situ* release of the reactive GA monomer,[7] as well as facilitating deprotonation of the linear TPP-ERU covalent adduct. Other protein electric field modulating mutations targeting the DHETPP dehydration reaction step are expected to improve catalytic activity toward both phosphorylated and nonphosphorylated substrates.

While saturation by the cyclic D-fructose nonphosphorylated substrate could not be experimentally observed in the Bad.F6Pkt H548N mutant with the previously reported highest initial reaction rate, k_{cat}/K_M for the acyclic ERU substrate was increased by approximately 1.6 fold compared to the wild-type enzyme, indicative of improved binding of the enzyme−substrate reaction TS.[9] H548 forms part of the binding site for the terminal phosphate group in the complex with the covalent F6P-TPP substrate adduct. The calculated respective upward shifts of +0.20 and +0.21 in the pK_a values of the H64 and D547 residue side chains in the H548N mutant (Table 1), although smaller, are comparable with corresponding shifts elicited upon introduction of the charged PO_4^{2-} ion surrogate for the 6-phosphate group in F6P. Stabilization of the D547 side chain carboxylate group by the mutant asparagine 548 side-chain carbamoyl group was identified as being mainly responsible for the rise in the predicted pK_a of D547. The electrostatic potential difference ($\Delta\varphi(\mathbf{r})$) map for the H548N mutant reveals local charge polarization in the enzyme reaction center and an increase in the electric field strength parallel to the axis of the covalent bond formed with the C2 TPP thiazolium ring carbon (Figure 3A).

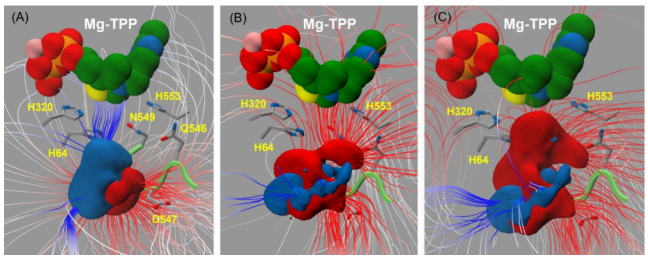

Figure 3. Electrostatic potential difference grid maps for Bad.F6Pkt variants carrying H548 mutation. (**A**) H548N, (**B**) H548Y, and (**C**) H260Y:H548Y. Difference electrostatic potential ($\Delta\varphi(\mathbf{r})$), calculated relative to wild-type Bad.F6Pkt, is displayed as solid rendered ± 2 kT/e contoured isosurfaces, colored in blue or red for positive or negative $\Delta\varphi(\mathbf{r})$, respectively. Electrostatic field lines, calculated at a fixed gradient magnitude setting, are colored according to the electrostatic difference potential and point away from positive charge difference sources. The Mg-TPP cofactor is shown as van der Waals spheres with green colored carbon atoms. Other atoms are colored according to element type: nitrogen, blue; oxygen, red; sulfur, yellow; phosphorus, orange. The Mg^{2+} ion is shown in pink. Active-site histidine (64, 320 and 553) and QN-loop (Q546, D547, H548, N549) residue side-chains are shown in stick-form with gray-colored carbons. The QN-loop mainchain is depicted in cartoon form as a lime green tube.

Electric Field Modulation as a Design Strategy to Improve BadF6PktBad.F6Pkt Activity toward GA

We next sought to identify electrostatic mutations with the potential to facilitate GA dimer ring opening both at long-range (Figure 4A) and at positions in the active-site center and substrate binding channel of the Bad.F6Pkt enzyme (Figure 2A). Electrostatic reorganization in mutants was evaluated from induced shifts in predicted pK_a values (ΔpK_a) at ionizable (reporter) residue positions, including those most influenced by the introduction of a PO_4^{2-} ion in the terminal F6P phosphate group binding site (Table 1), and by visual inspection of the corresponding ($\Delta\varphi(\mathbf{r})$) electrostatic potential difference maps and field line density at the active-site center. Candidate replacement residue type selection was assisted by position-specific frequency profiles of tolerated residue substitution and statistical correlation energy measures of pairwise residue type dependence determined by analysis of a multiple sequence alignment of PKT enzyme family members (see Methods).

1. Long-Range Mutations at T2, I6, H256, and H260 Positions. Long-range H260Y and T2A:I6T Bad.F6Pkt mutations identified by random mutagenesis were reported by Dele-Osibanjo et al.[74] to increase k_{cat}/K_M toward F6P. A further enhancement in catalytic efficiency could be obtained by combining mutations at the three sites in the same region close to the enzyme surface approximately 29 Å (H260Y) and

https://doi.org/10.1021/acs.jpcb.6c02050
J. Phys. Chem. B 2026, 130, 7791−7808

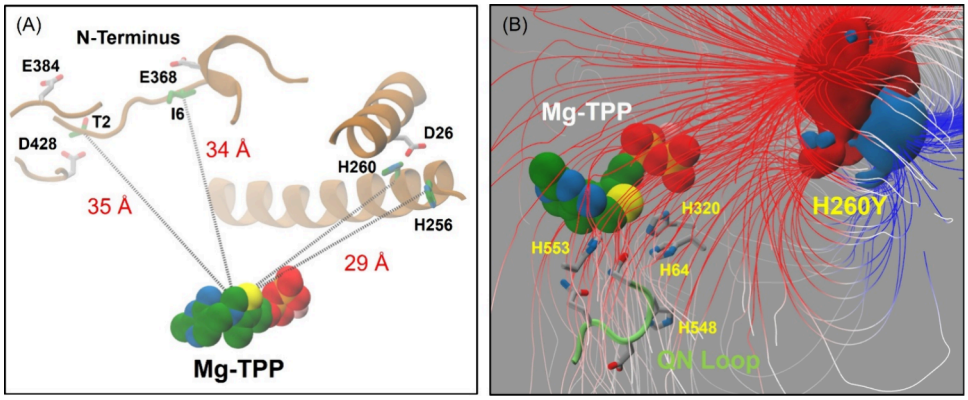

Figure 4. Long range electrostatic mutations in Bad.F6Pkt. (**A**) Locations of mutated residues (green side-chain carbons) and proximal acidic residues (gray side-chain carbons) with respect to the Mg-TPP cofactor in the enzyme catalytic center. Mg-TPP is depicted with space filling van der Waals spheres colored according to element type: carbon, green; nitrogen, blue; oxygen, red; sulfur, yellow; phosphorus, orange; magnesium, pink. Distance separations between the TPP C2 thiazolium ring atom and C^{α} atoms of mutated enzyme residues are annotated in red. (**B**) H260Y mutant electrostatic potential difference grid map. Solid rendered ± 2 kT/e contoured isosurfaces are colored in blue or red for positive or negative difference potential, respectively. Electrostatic field lines, calculated with the same gradient magnitude setting as in Figure 3, are colored according to the electrostatic difference potential due to mutation. Histidine (64, 320 and 553) and QN-loop (Q546, D547, H548, N549) residue side-chains in the active-site are shown in stick-form with gray-colored carbons. The QN-loop mainchain is depicted in cartoon form as a lime green tube.

34 to 35 Å (T2A:I6T) removed from the active-site. Interestingly no changes in K_M were observed, indicating that the increases in catalytic efficiency derived directly from favorable increases in reaction TS binding rather than substrate ground-state binding. The exhibition of relatively larger mutant rate enhancements toward F6P as compared to the acyclic X5P substrate[74] is consistent with a lowering of the reaction energy barrier for ring opening, although differential effects on the deprotonation of the substrate TPP covalent adducts cannot be ruled out. Mutation induced changes to the protein electric field in the active-site are illustrated in Figure 4B (H260Y) and Figure S5 (T2A:I6T). In contrast to the H548N mutant (Figure 3A), charge polarization due to mutation leads to an excess of negative electrostatic potential in the catalytic center. Whereas catalytic field modulation arising from the long-range H260Y mutation is confined to the closest active-site center in the Bad.F6Pkt dimer, perturbation of the electric field can be observed in both catalytic centers in the T2A:I6T long-range double mutant.

Analysis of predicted ΔpK_a data in long-range electrostatic mutations (Table S2) did not reveal any change in pK_a values of ionizable residue side-chains in the active site. An increase of 0.45 in the predicted side-chain pK_a of D27 was observed in the H260Y mutant. The partially buried D27 residue position lies on an adjacent α-helix to H260 which shields the carboxylate side-chain from the solvent (Figure 4A). Although histidine is the most prevalent residue type at this position in the PKT family multiple sequence alignment (MSA), tyrosine is well-represented (Figure S7). A similar local environmental change accompanying tyrosine mutation of H256, located at the N-terminus of the same helix as H260, increased the predicted D27 side chain pK_a of D27 by 0.32 units. Proline is the most frequently observed residue type at position 256 in the PKT family MSA (Figure S7), and a similar D27 side chain ΔpK_a value of +0.33 was calculated in the H256P mutant. Mutation induced increases in the predicted D27 side-chain pK_a at positions 256 and 260 were additive, and a ΔpK_a value of 0.79 was recorded for the H256Y:H260Y double mutant. Acidic aspartate and glutamate residues account for 62% of all sequence-weighted residue type counts at position 27 in the PKT family MSA (Figure S7). In contrast, in the T2A:I6T double mutant, no acidic residue side chain pK_a shifts were observed in reporter positions close to the T2 (E384 and D428) and I6 (E368) mutation sites (Figure 4A).

2. Substrate Binding Channel Mutations at D56, H142, E153, D547, H548, and N549 Positions. Exploratory investigation of electrostatic reorganization arising from mutations at D547 (H_x = 0.37), H548 (H_x = 0.17), and N549 (H_x= 0.03) positions displaying varying degrees of conservation in the mobile QN-loop in the active-site principally led to the identification of H548Y as the most promising candidate. Predicted pK_as of the imadazole side-chains of H64, H320, and H553 histidine residues suggested in the literature to be the PKT B_2 catalyst[53,58,59] were respectively shifted upward by 0.32, 0.10, and 0.11 units in H548Y (Table 1). The ΔpK_a shift for the H64 side chain able to hydrogen bond with the O1 ring oxygen atom of the bound GA-dimer (Figure 2B) is notably increased compared to the H548N mutant (Table 1). This is accompanied by a positive to negative reversal in the induced polarized electrostatic charge difference in the catalytic reaction center, discernible from electrostatic potential difference maps for the H548N (Figure 3A) and H548Y (Figure 3B) mutants. The predicted side chain pK_a of the adjacent D547 residue shifted identically by +0.21 in both mutants (Table 1). Exploitation of the differences in side-chain size and pK_as of aspartate (4.0) and glutamate (4.4) in model compounds[70] was examined as a possible means of fine-tuning of the local electric field in the active-site, noting also that glutamate and aspartate are approximately equally represented at position 547 in the PKT family (Figure S7). Although the ΔpK_a for the residue side-chain at position 547 was raised by +0.79 in the H548Y:D547E double mutant, calculated shifts in the H64, H320, and H553 histidine side-chain pK_as remained almost unchanged (Table S3). Replacement of N549 with a negatively charged aspartate residue was predicted to be effective in raising the side-chain pK_as of almost all the basic residues in the active site, including H64 by almost one unit (Table S4). Among the calculated pK_a perturbations caused by the introduction of cysteine, serine, and valine replacements at position 549, documented in Table S4, the only active-site

https://doi.org/10.1021/acs.jpcb.6c02050
J. Phys. Chem. B 2026, 130, 7791−7808

Table 2. Kinetic Parameters of Bad.F6Pkt Wild Type and Selected Variants

	D-erythrulose			glycolaldehyde		
Bad.F6Pkt	V_{max} [U mg^{-1}]	K_M [mM]	k_{cat}/K_M [M^{-1} s^{-1}]	V_{max} [U mg^{-1}]	K_M [mM]	k_{cat}/K_M [M^{-1} s^{-1}]
wild type[a]	0.30 (±0.09)	36.2 (±3.2)	13.1 (±4.5)	0.41 (±0.09)	n.sat.	n.d.
H548N[a]	0.67 (±0.12)	48.7 (±0.4)	21.3 (±3.6)	0.53 (±0.03)	n.sat.	n.d.
H548Y	0.62 (±0.08)	26.9 (±1.9)	35.4 (±4.3)	0.41 (±0.02)	43.4 (±3.5)	14.8 (±1.0)
H260Y:H548Y	0.75 (±0.06)	21.2 (±1.7)	54.9 (±1.9)	0.50 (±0.02)	40.9 (±1.2)	19.0 (±1.1)
H256Y:H260Y:H548Y	0.59 (±0.08)	16.9 (±1.4)	49.6 (±7.8)	0.48 (±0.05)	40.3 (±2.3)	19.1 (±0.8)
H142N[b]	0.07 (±0.01)	9.0 (±0.3)	11.6 (±2.0)	0.58 (±0.13)	42.3 (±3.2)	20.6 (±3.9)
H142N:E153D	0.03 (±0.00)	4.9 (±1.8)	9.4 (±2.4)	0.08 (±0.01)	4.4 (±0.2)	26.3 (±3.3)

Experiments were carried out at pH 6.5, 37 °C in the presence of 50 mM sodium phosphate. If substrate saturation was not observed under the experimental conditions (n.sat.), it was not possible to determine K_M, and consequently, the catalytic efficiency k_{cat}/K_M could not be calculated (n.d.). Deviation of the mean is given in parentheses ($n \geq 2$). [a]Data reproduced from ref.[9] Available under a CC-BY 4.0 license. Copyright Kraußer et al. V_{max} values for glycolaldehyde refer to the specific activity at a substrate concentration of 300 mM, since no saturation was observed under tested conditions. [b]Data were obtained in this work. Mutation H142N has been studied previously by Yang et al.[6]

histidine residue with a higher side-chain pK_a than in the H548Y mutant was H553 in the H549S mutant (ΔpK_a = +0.19).

The H142N catalytic center mutant was recently isolated by Yang et al.[6] from random pairwise residue type combination library screening at five positions (P136, H142, S440, R524, and S739) with improved catalytic efficiency toward both GA and ERU compared to the Bad.F6Pkt wild-type enzyme. Asparagine is observed at low frequency (0.4%) at the highly conserved 142 position (H_X = 0.06) in the PKT family sequence alignment (Figure S7). Significant predicted shifts in the H64 (+0.34) and H553 (+0.21) residue side-chain pK_a values were observed for this mutant (Table 1), as well as an evident increase in the electric field strength close to the C2 atom of the TPP cofactor (Figure S6A). The side chain pK_a of the nearby E153 residue, to which we previously drew attention,[9] was calculated to increase by 0.21 units in an analogous fashion to that of D547 in the H548N and H548Y mutants (Table 1). Replacement of E153 by an aspartate residue in the H142N:E153D double mutant led to further calculated ΔpK_a increases for H64 (+0.39) and H553 (+0.27) histidine side-chains, in addition to a predicted rise of +0.11 in the H97 side-chain pK_a, unobserved in any other mutant examined here (Table 1).

In a further attempt to influence the protein electric field in the active site from a longer distance, D56 situated at the entrance of the substrate binding channel (Figure 2A) was replaced by an isosteric asparagine residue tolerated at this position in the PKT family (Figure S7). Although the predicted side-chain pK_a of the nearest acidic residue (E55) was lowered by 0.12 unit, no changes were found in the calculated side-chain pK_a values of histidine residues in the catalytic center (Table S4).

Introduction of Long-Range Mutation Increases Catalytic Efficiency for GA and ERU

To facilitate experimental investigation of electrostatic mutation combinations primarily aimed at promoting GA dimer ring opening, we first sought to identify an alternative background to the H548N mutant as a basis for engineering. Taking into account the size and conformational differences in preferred ring forms adopted by the GA dimer (β-furanose) and D-fructose (β-pyranose), we therefore screened the 20 active-site variants previously reported to enhance D-fructose activity[9] for their activity on GA (see Figure S9). The PKT mutants were expressed using the *E. coli* Rosetta (DE3) plysS strain and pET-28(a)+ expression vector harboring the corresponding gene with an N-terminal His-tag. Proteins were purified, and their activity was tested using the colorimetric hydroxamate assay, that detects the phosphoketolase reaction product acetyl-P.[50,51] The H548Y Bad.F6Pkt variant exhibited significantly improved catalytic performance toward the C_2 aldehyde and ERU compared to both the wild-type enzyme and the H548N variant (Table 2). The H548Y Bad.F6Pkt electrostatic mutant was therefore preferred as a more suitable single mutational variant background in addition to the wild-type enzyme for combinatorial engineering at residue positions highlighted in Figure 2A and Figure 4A.

Several of the single Bad.F6Pkt mutants computationally investigated for evidence of improved electrostatic preorganization were then experimentally assessed for their influence on GA and ERU activity (Figure S10). Kinetic parameters determined for selected variants are shown in (Figure 5). Consistent with previous observations for F6P and fructose,[9]

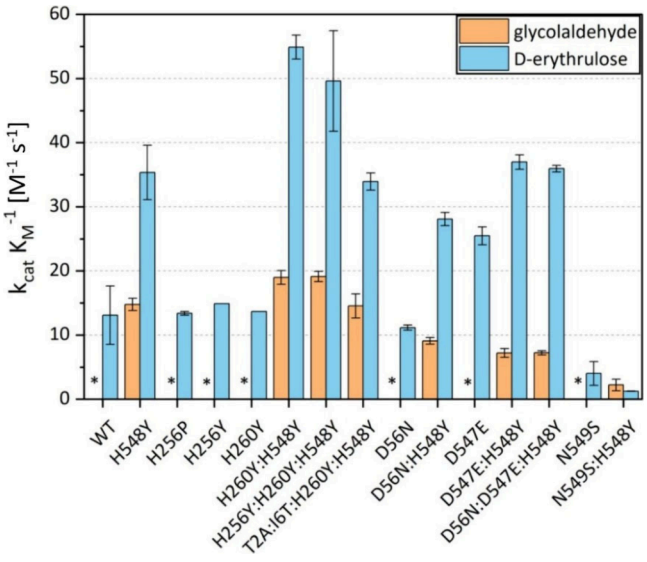

Figure 5. Bad.F6Pkt variant catalytic efficiency k_{cat}/K_M for D-erythrulose and glycolaldehyde. WT − wild type. Experiments were carried out at pH 6.5, 37 °C in the presence of 50 mM sodium phosphate. Nonlinear kinetic parameter fitting of experimental data to the Michaelis−Menten equation was carried out using MATLAB R2023b. In cases where substrate saturation could not be observed under experimental conditions, it was not possible to determine K_M or k_{cat}/K_M (*). Error bars indicate deviation of the mean ($n \geq 2$).

https://doi.org/10.1021/acs.jpcb.6c02050
J. Phys. Chem. B 2026, 130, 7791−7808

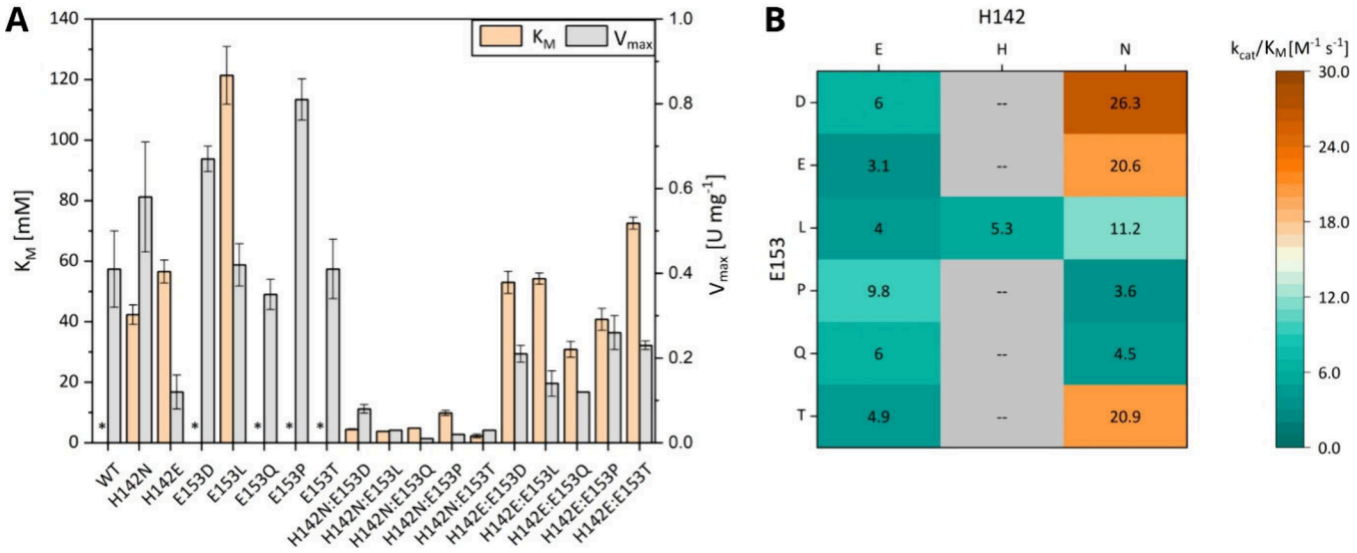

Figure 6. Kinetic parameters of Bad.F6Pkt H142-E153 mutants for glycolaldehyde. A) Michaelis−Menten constant K_M for glycolaldehyde and maximum specific activity V_{max}. WT − wild type. Experiments were carried out at pH 6.5, 37 °C in the presence of 50 mM sodium phosphate. Nonlinear kinetic parameter fitting of experimental data to the Michaelis−Menten equation was performed using MATLAB R2023b. If no substrate saturation was observed under tested conditions, K_M could not be determined (*), and the specific activity at a substrate concentration of 300 mM is given as V_{max}. Error bars indicate deviation of the mean ($n \geq 2$). **B)** Catalytic efficiency k_{cat}/K_M for glycolaldehyde. − In the absence of a K_M estimate, k_{cat}/K_M cannot be determined. Values represent the mean of at least two replicates.

mutations at the highly conserved N549 position (D,C,S,V) resulted in a substantial decline in ERU and GA activity (Figure S10). While the single variants H256P, H256Y, H260Y, and D56N exhibited catalytic properties comparable to those of the wild-type enzyme for both substrates, D547E increased catalytic efficiency on the C_4 sugar by a factor of 1.9 (Figure 5) and GA activity by 33 ± 4% (Figure S10). However, substrate saturation was not observed at concentrations of up to 300 mM GA in these single variants.

Substitution of H548 by a larger aromatic tyrosine residue in this study permitted the only experimental determination of a mutant k_{cat}/K_M kinetic parameter for glycolaldehyde at this position. Although a k_{cat}/K_M specificity constant parameter value could not be experimentally obtained for the H548N mutant on the GA substrate, it is reasonable to suppose the relative improvement in k_{cat}/K_M for the H548Y mutant on the same substrate is significantly larger than experimentally determined ratio of 1.7 for the linear ERU substrate (Table 2). These kinetic data are consistent with GA dimer ring opening no longer being rate-limiting in the H548Y mutant provided it is further assumed that any increase in catalytic performance toward the acyclic monomeric GA species for this mutant is on the same order as that for ERU. The catalytic efficiency of the Bad.F6Pkt variant H548Y was further enhanced by 28% for GA and 55% for ERU through the introduction of a tyrosine residue in position H260 (Figure 5, Table 2). Comparison of the electrostatic potential difference maps for the H548Y (Figure 3B), H260Y (Figure 4B), and H548Y:H260 (Figure 3C) mutants illustrates constructive addition of the individual mutation-induced modulations of the protein electric field in the double mutant. The additional replacement of histidine 256 by a tyrosine did not influence the kinetic parameters for GA or the k_{cat}/K_M for ERU. Nevertheless, we continued to work with the triple mutant H256Y:H260Y:H548Y, as the introduction of the third tyrosine residue significantly decreased the K_M value for the C_4 sugar to 16.9 ± 1.4 mM (Table 2).

GA Affinity of Bad.F6Pkt H142N Enhanced by Introduction of Additional E153D Mutation

Yang et al. recently identified a Bad.F6Pkt active-site variant, H142N, which exhibited a 2-fold higher V_{max} than the wild-type enzyme and a K_M value of 11.6 mM for GA at pH 7.5.[6] Although the kinetic parameters obtained under the experimental conditions of the present study differed (we applied pH 6.5), the beneficial effect of the H142N mutation on GA activity and affinity was confirmed. The catalytic efficiency of the H142N mutant for GA was found to be comparable to the H260Y:H548Y and H256Y:H260Y:H548Y variants described above (Table 2). In accordance with previous observations by Yang et al., the H142N variant exhibited a reduced K_M value for ERU as well as impaired maximum activity in comparison to the wild-type enzyme (Table 2).

To explore potential synergistic effects on GA and ERU activity, we first combined the H142N mutation with previously identified substitutions shown to enhance activity or affinity toward nonphosphorylated substrates. These included H548N,[9] Q546E:N549D,[9] H548Y, H260Y:H548Y, and H256Y:H260Y:H548Y. However, the majority of the resulting Bad.F6Pkt H142N variants exhibited a loss of activity toward both target substrates (Figure S11). The field line spatial disposition in the electrostatic potential difference map for the H142N:H548Y double mutant provides evidence of the counterproductive combined neutralization of individual mutation-induced polarized charge in the immediate vicinity of the TPP cofactor C2 atom (Figure S6C). Only the combination of H142N with H256Y resulted in a slight increase in GA activity compared to the corresponding single variant (Figure S11).

Experimentally observed enhanced GA activity of the H142N mutant can be correlated with calculated upward shifts in the pK_as of putative B_2 catalyst H64 and H553 residue side chains (Table 1) and reorganization of the electric field in the active-site center (Figure S6A). In common with mutation-targeted histidine residues at positions 256, 260, and 548 that

https://doi.org/10.1021/acs.jpcb.6c02050
J. Phys. Chem. B 2026, 130, 7791−7808

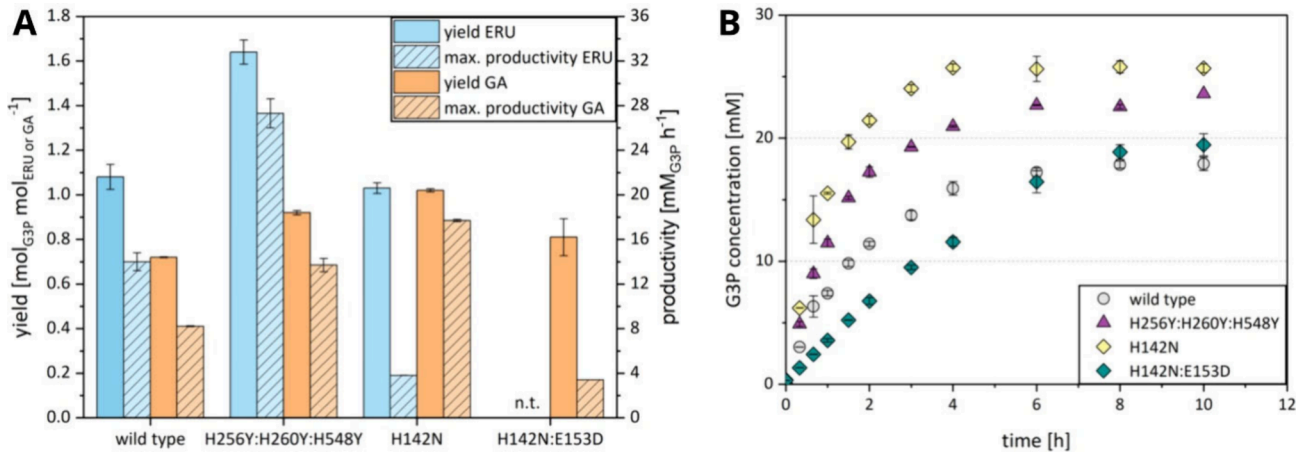

Figure 7. ***In vitro*** **ATP regeneration from either ERU (blue) or GA (orange) by a phosphoketolase. A)** *In vitro* sn-glycerol 3-phosphate (G3P) yield and productivity with ATP regenerated from ERU or GA using different Bad.F6Pkt variants or the wild-type enzyme. **B)** G3P production by different Bad.F6Pkt variants or the wild-type enzyme using GA as substrate. **A) + B)** Experiments were carried out at pH 7.0, 37 °C in the presence of 50 mM sodium phosphate and glycerol, 0.8 mM TPP, 4 mM $MgCl_2$, 1 mM ADP, and a starting concentration of 25 mM D-erythrulose or glycolaldehyde. Phosphoketolase activity was modulated by employing either wild-type Bad.F6Pkt or indicated variants at a concentration of 2 mg mL^{-1}. n.t. – not tested. Data represent mean and deviation of biological duplicates.

screen centers of negative charge in proximal aspartate side-chains, mutation of H142 to asparagine led to a predicted increase in the side-chain pK_a of the partially buried nearby E153 acidic residue (Table 1). Multiple sequence alignment weighted frequency profile analysis shows the presence of acidic glutamate residues in 93% of PKT family sequences at this largely invariant (H_x = 0.14) position (Figure S6). Aspartate residues are notably poorly represented (0.8%) at position 153 in native PKTs with preferred specificities for phosphorylated substrates. E153 thus represents a promising target for further enhancement of GA activity and affinity in the Bad.F6Pkt H142N variant. Guided by a hierarchical clustered statistical correlation energy heat map for positions 142 and 153 (Figure S8) derived from MSA data (see Methods), a focused H142-E153 double mutant library was generated and assessed for GA and ERU activity. It comprised the residues D, L, P, Q, and T and the wild-type in position E153, as well as asparagine, glutamate, and the wild-type histidine in position 142 (Figure 6B).

As observed for the Bad.F6Pkt H142N single mutant (Table 2), all tested H142-E153 double mutants exhibited a decrease in ERU activity of at least 60% in comparison to the wild-type enzyme, along with a significant reduction in catalytic efficiency toward the C_4 sugar (data not shown). The introduction of either glutamate or asparagine in position H142 of the Bad.F6Pkt E153 variants was found to significantly decrease V_{max} for GA (Figure 6A). However, the asparagine residue conferred a pronounced improvement in GA affinity, with K_M values for the H142N:E153 variants approximately 1 order of magnitude lower than those of the corresponding single mutants (Figure 6A). Among these, only Bad.F6Pkt H142N:E153D exhibited higher catalytic efficiency for the C_2 aldehyde than the H142N single mutant, which was increased by approximately 28% (Figure 6B, Table 2). A K_M value of 4.4 ± 0.2 mM was observed for this double mutant, corresponding to a 10-fold higher GA affinity compared to H142N (Figure 6A, Table 2). A marked reduction in V_{max} accompanying the significant lowering of the Michaelis constant is characteristic of the preferential stabilization of the substrate ground-state over the reaction transition-state. Comparison of the electrostatic potential difference maps shown in Figure S6 for the H142N (A) and H142N:E153D (B) mutations reveals the clear displacement of high-density field line zones associated with improved catalytic activity away from the enzyme reaction center in the double mutant.

Bad.F6Pkt Variants Improve the Performance of ATP Synthesis from Either GA or ERU

Practical advantages provided by the newly constructed enzymes were investigated using *in vitro* ATP regeneration from GA or ERU as a model system. The reaction system produced *sn*-glycerol 3-phosphate (G3P) from glycerol and ATP using glycerol kinase from *Cellulomonas sp.* NT3060 (Cs.GlpK). Acetate kinase from *Geobacillus stearothermophilus* (Gs.AckA) was employed to enable ATP regeneration from ADP. Both enzymes were previously found to be highly active and stable under synthesis-like conditions.[9,75,76] PKT activity in the reaction systems was modulated by employing either the Bad.F6Pkt wild-type enzyme or selected variants with enhanced kinetic parameters for ERU and/or GA at a concentration of 2 mg mL^{-1}. The ATP-dependent G3P production was assessed using an initial concentration of 25 mM ERU or GA, 1 mM ADP, and an excess of glycerol and phosphate (50 mM, respectively).

First, we evaluated the G3P synthesis from GA by the GA-specific Bad.F6Pkt variants H256Y:H260Y:H548Y, H142N, and H142N:E153D in comparison with the wild-type enzyme. The reaction employing the Bad.F6Pkt H142N:E153D variant proceeded for 10 h, resulting in a final G3P concentration of 19.5 ± 0.9 mM and a slightly increased yield (0.8 ± 0.08 mol_{G3P} mol_{GA}^{-1}) compared to the wild-type (0.7 ± 0.00 mol_{G3P} mol_{GA}^{-1}) (Figure 7). Further, it was observed that reactions containing the wild-type PKT or the H256Y:H260Y:H548Y mutant ceased G3P production after 6 h, reaching final product concentrations of 17.9 ± 0.5 mM and 22.7 ± 0.3 mM, respectively (Figure 7B). This incomplete substrate conversion may be attributed to PKT inactivation in the presence of GA.[27] In contrast, complete conversion of the limiting substrate GA to G3P was achieved within 4 h using the Bad.F6Pkt H142N variant (Figure 7), thus demonstrating the feasibility of *in vitro* ATP regeneration from the

https://doi.org/10.1021/acs.jpcb.6c02050
J. Phys. Chem. B 2026, 130, 7791−7808

Table 3. Properties of Enzymes Used for *In Vitro* Acetyl-P Synthesis

Enzyme	Go.Gox0313	Ms.Nox	Ec.FsaA L107Y:A129G	Ps.LrhI
Organism	*Gluconobacter oxidans*	*Methanobrevibacter smithii*	*Escherichia coli*	*Pseudomonas stutzeri*
Function	ethylene glycol dehydrogenase	NADH oxidase	D-threose aldolase	threose isomerase
V_{max} [U mg^{-1}]	0.14 ± 0.02[a]	0.03 ± 0.00	5.3 ± 0.3[d]	1.0 ± 0.2
K_M [mM]	n.sat. (EG)	0.05−0.06 (NADH)[c]	0.09 ± 0.01 (GA, donor)[d]	25.7 ± 3.2 (D-threose)
	0.06 (NAD^+)[b]	0.02 (O_2)[c]	2.1 ± 0.3 (GA, acceptor)[d]	
K_{eq}	7.0 × 10^{-5}	1.1 × 10^{40}	670	3

Unless otherwise stated, kinetic parameter data obtained in this work represent mean values and standard deviation from at least two experiments carried out at 37 °C and pH 7.0. The equilibrium constant K_{eq} was determined using the web tool eQuilibrator 3.0[78] with the following settings: pH 7.0, pMg 3.0, and ionic strength 0.25 M. n.sat. − no substrate saturation. [a]V_{max} refers to the specific activity at an ethylene glycol concentration of 100 mM, since no saturation was observed under the tested conditions. [b]Parameters estimated at pH 8.5 and 30 °C.[79] [c]Parameters estimated at pH 7.2.[80] [d]Parameters estimated at pH 7.5 and 25 °C.[31,81]

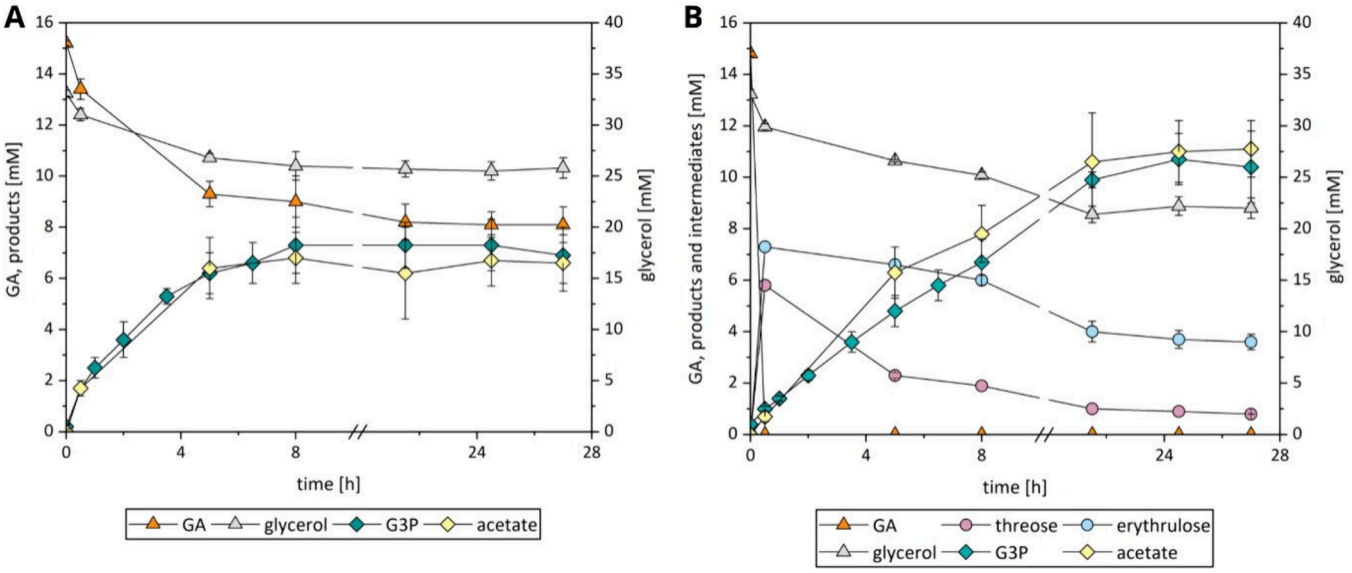

Figure 8. Glycolaldehyde (GA) conversion in phosphoketolase-based reaction systems for *in vitro* ATP regeneration. A) Course of substrate and product concentrations over time using 0.2 mg mL^{-1} Bad.F6Pkt H256Y:H260Y:H548Y for acetyl-P production. **B)** Course of substrate, intermediate, and product concentrations over time using 0.2 mg mL^{-1} Bad.F6Pkt H256Y:H260Y:H548Y in combination with 0.33 mg mL^{-1} Ec.FsaA L107Y:A129G and 2.5 mg mL^{-1} Ps.LrhI for acetyl-P production. **A) + B)** Experiments were carried out at pH 7.0, 37 °C in the presence of 32 mM sodium phosphate and glycerol, 0.8 mM TPP, 4 mM $MgCl_2$, 1 mM ADP, and a starting concentration of 15 mM glycolaldehyde. Data represent mean and deviation of biological duplicates.

nonphosphorylated C_2 aldehyde. Notably, the utilization of Bad.F6Pkt H142N also resulted in the highest maximum G3P productivity of 17.7 ± 0.1 mM h^{-1}, consistent with its comparatively high V_{max} (Figure 7A, Table 2). Despite its improved GA affinity, the double Bad.F6Pkt mutant H142N:E153D possessed a significantly lower kinetic turnover number compared to H142N (Table 2), reflected by its inability to outperform the single variant in terms of ATP regeneration from an initial GA concentration of 25 mM.

After demonstrating the GA-based ATP regeneration system, we sought to investigate whether the *in vitro* synthesis of up to two mol ATP from one mole ERU via the intermediate GA (as shown in Figure 1) is feasible. Here, the performance of the ERU-specific Bad.F6Pkt variant H256Y:H260Y:H548Y was compared with the wild-type enzyme. The single mutant H142N was included as a control, as it enabled complete conversion of GA that is present as an intermediate in the ERU-based ATP regeneration system. ATP regeneration from 25 mM ERU using the Bad.F6Pkt H256Y:H260Y:H548Y variant enabled the synthesis of up to 40.2 ± 1.3 mM G3P within 6 h (Figure S12A). This corresponds to a yield of 1.64 ± 0.05 mol_{G3P} mol_{ERU}^{-1}, demonstrating that both the PKT-catalyzed conversion of ERU to acetyl-P and the subsequent degradation of the resulting GA intermediate contributed to ATP regeneration in this system (see Figure 1). Furthermore, a maximum productivity of 27.3 ± 1.3 mM h^{-1} was achieved with the Bad.F6Pkt triple mutant, which is nearly twice that observed with the wild-type enzyme (Figure 7A). In contrast, utilization of the wild-type Bad.F6Pkt or the H142N variant resulted in significantly lower productivity and smaller yields of approximately 1 mol_{G3P} mol_{ERU}^{-1}, as G3P synthesis ceased after six and 8 h, respectively (Figure 7A, Figure S12A). It is noteworthy that only the use of the H256Y:H260Y:H548Y mutant identified in this study led to near-complete consumption of the C_4 sugar substrate (residual ERU concentration was 2.1 ± 0.1 mM). In the same reaction, up to 7 mM GA were accumulated (Figure S12B).

Coupling of Threose Aldolase and Threose Isomerase with ERU-Specific PKT Enables Rapid Conversion of GA and Increases the ATP Yield

Following the successful demonstration of ATP regeneration from ERU and GA, respectively, we set out to investigate

https://doi.org/10.1021/acs.jpcb.6c02050
J. Phys. Chem. B 2026, 130, 7791−7808

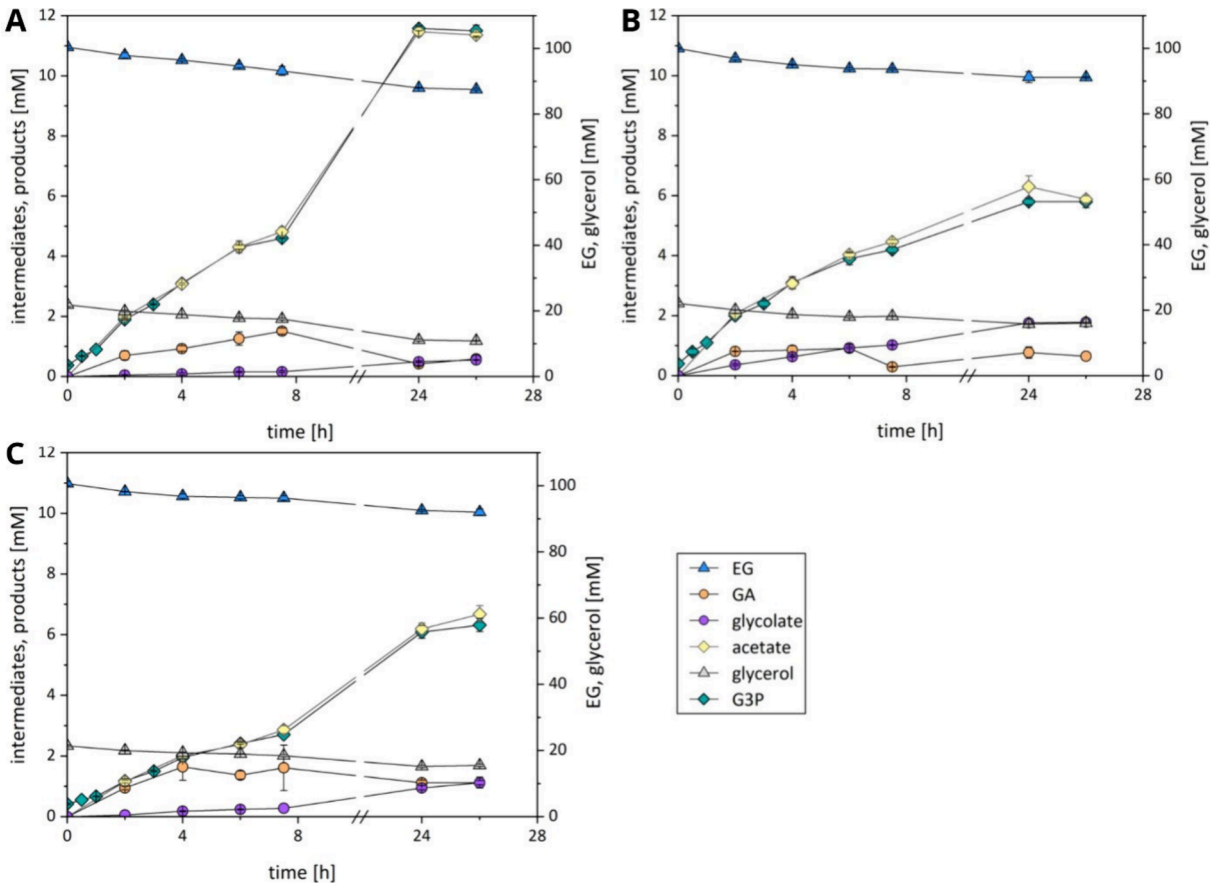

Figure 9. ***In vitro*** **sn-glycerol 3-phosphate (G3P) synthesis with a reaction system for ATP regeneration based on ethylene glycol.** Substrate consumption, accumulation of intermediates and (by-) products during *in vitro* G3P synthesis using 2 mg mL^{-1} **A**) Bad.F6Pkt H142N, **B**) Bad.F6Pkt H142N:E153D, or **C**) the wild-type phosphoketolase enzyme in combination with 0.5 mg mL^{-1} Go.Gox0313 and 1.4 mg mL^{-1} Ms.Nox for acetyl-P production. Experiments were carried out at pH 7.0, 37 °C and 200 rpm in the presence of 0.8 mM TPP, 4 mM $MgCl_2$, 2 mM NAD^+, and 1 mM ADP, with initial concentrations of 100 mM ethylene glycol, 32 mM sodium phosphate, and 22 mM glycerol. Data represent mean and deviation of biological duplicates.

whether incorporating a D-threose aldolase and D-threose isomerase into the reaction system could enhance ATP yield from GA by accelerating the degradation of the enzyme-inactivating C_2 aldehyde (see Figure 1). The *E. coli* fructose 6-phosphate aldolase (Ec.FsaA) variant L107Y:A219G was employed for the conversion of two molecules of GA to one molecule of D-threose, due to its reported high activity and affinity for GA.[31] The D-threose isomerase activity was provided by L-rhamnose isomerase from *Pseudomonas stutzeri* (Ps.LrhI),[77] for which kinetic parameters were determined (Table 3). *In vitro* G3P synthesis from 15 mM GA by glycerol kinase, acetate kinase, and the Bad.F6Pkt variant H256Y:H260Y:H548Y was evaluated in the presence and absence of threose aldolase and isomerase. The PKT triple mutant was utilized in both reactions at a concentration of 0.2 mg mL^{-1}, due to its beneficial properties regarding ERU and GA, respectively.

Without conversion of GA to threose and ERU, G3P synthesis ceased after 8 h (Figure 8A). With approximately half of the initial GA concentration remaining, the observed loss of PKT activity can be attributed to enzyme inactivation caused by the aldehyde (ref 27, Table S6). In contrast, in the presence of threose aldolase and isomerase, complete consumption of GA occurred within less than 30 min. The transient accumulation of the intermediates threose and ERU (Figure 8B) indicated that the coupling of threose aldolase and isomerase enabled the conversion of GA to ERU through the intended pathway (Figure 1). The performance of the reaction system was significantly improved, as witnessed by the G3P yield which increased from 0.47 ± 0.06 mol_{G3P} mol_{GA}^{-1} to 0.69 ± 0.06 mol_{G3P} mol_{GA}^{-1} (Figure 8). However, a complete conversion of GA to G3P was not achieved, and the reaction ceased with 0.8 ± 0.0 mM D-threose and 3.6 ± 0.3 mM ERU remaining in the reaction mix. As previously reported for its diastereomer D-erythrose,[9] D-threose also irreversibly inactivates the PKT enzyme, reducing its half-life from 144 h[9] to 19.7 h at a concentration of 10 mM. Although the pseudo-first order rate constant for inactivation by D-threose is approximately 1 order of magnitude lower than that of GA when present at the same molar concentration (Table S6), the incomplete conversion of GA to G3P can likely be attributed to irreversible inactivation of the PKT by D-threose.

ATP Regeneration from Ethylene Glycol Is Enhanced by Improved PKT Variants

As illustrated in Figure 1, GA is proposed to be generated *in situ* from the less toxic[10] and less expensive bulk chemical ethylene glycol (EG) in the envisioned ATP regeneration system(s). Based on literature reports, EG dehydrogenase from *Gluconobacter oxidans* (Go.Gox0313)[79,82,83] and NADH oxidase from *Methanobrevibacter smithii* (Ms.Nox)[80] were selected for the oxidation of EG to GA and characterized in

https://doi.org/10.1021/acs.jpcb.6c02050
J. Phys. Chem. B 2026, 130, 7791−7808

terms of their activity at synthesis-like conditions (pH 7.0, 37 °C) (Table 3). As both enzymes exhibited adequate activities, they were subsequently combined with a GA-specific PKT variant, acetate kinase, and glycerol kinase to assess the functionality of the *in vitro* reaction system for ATP regeneration from EG (as shown in Figure 1). The two Bad.F6Pkt variants with the highest catalytic efficiency for GA (H142N and H142N:E153D) were compared to the wild-type enzyme, in order to investigate whether employing a GA-specific PKT could enhance the reaction system performance. Given that GA reduction is thermodynamically favored over EG oxidation (Table 3[10,79]), EG was supplied in excess (100 mM), while glycerol (22 mM) served as the limiting substrate for *in vitro* G3P synthesis.

Compared to the wild-type Bad.F6Pkt, employing the GA-specific variants H142N or H142N:E153D resulted in a 2-fold higher G3P productivity during the initial 7 h of the reaction (Figure 9), reaching a maximum of 0.78 mM h^{-1}. The utilization of the Bad.F6Pkt variant H142N increased the overall G3P yield from 0.28 ± 0.02 mol_{G3P} $mol_{glycerol}^{-1}$ (wild-type enzyme) to 0.52 ± 0.02 mol_{G3P} $mol_{glycerol}^{-1}$. In contrast, a precipitate was observed in reaction mixtures containing Bad.F6Pkt H142N:E153D after 6 h, which, together with halted conversion of GA (inferred from stagnating acetate and G3P concentrations), indicates reduced stability of the double mutant under synthesis conditions. The highest GA accumulation occurred in the reaction employing the wild type PKT (1.1 ± 0.1 mM), followed by the double and the single mutant (0.8 ± 0.2 mM and 0.4 ± 0.1 mM).

DISCUSSION

In this study, we successfully applied a rational electrostatic enzyme engineering design approach to improve the affinity and catalytic efficiency of PKT from *B. adolescentis* for the nonphosphorylated substrates ERU and GA. Additionally, we implemented an *in vitro* ATP regeneration system, which is based on the oxidation of the bulk chemical EG to GA and subsequent production of the high-energy phosphoryl donor acetyl-P by an engineered PKT. Efficient conversion of the cell-toxic intermediate GA was achieved *in vitro* either by employing a GA-specific PKT variant or, alternatively, by coupling D-threose aldolase and D-threose isomerase with an ERU-specific PKT in the presence of inorganic phosphate.

Engineering of the wild-type PKT was focused on promotion of *in situ* ring-opening of the cyclic GA dimer and the generation of the reactive monomeric form[7] to enhance substrate specificity for the C_2 aldehyde. Molecular modeling of the Bad.F6Pkt−TPP complex with bound cyclic GA dimer, combined with multiple sequence alignment analysis and calculations of side-chain pK_a shifts at ionizable protein residues, enabled the identification of electrostatic mutations in two distinct regions of the enzyme that could facilitate GA dimer ring opening. Whereas the wild-type Bad.F6Pkt showed no substrate saturation up to 300 mM GA, substitution of the active-site residue H548 by a larger aromatic tyrosine permitted experimental determination of a k_{cat}/K_M kinetic parameter for GA and increased the catalytic efficiency for ERU by a factor of 2.7. Improved catalytic performance toward GA and ERU could be correlated with predicted upward shifts in H64, H320, and H553 side-chain pK_a values that appear to at least partially mirror those induced in native PKTs by the terminal phosphate groups of cognate X5P and F6P phosphorylated substrates. Introduction of the long-range mutation H260Y into the H548Y background further enhanced catalytic efficiency for both GA and ERU, as predicted by the constructive modulation of the protein electric field in the enzyme catalytic center (Figure 3). With a 4.2-fold higher k_{cat}/K_M than the wild-type enzyme, this double mutant exhibited the highest catalytic efficiency for the open-chain ERU reported to date.[6,9] This may be tentatively attributed to a lowering of TS energy barriers for deprotonation of the bound TPP-ERU covalent adduct or the dehydration step by the double mutant. Additional replacement of histidine 256 by a tyrosine did not affect GA kinetics but slightly improved ERU binding without significantly altering k_{cat}/K_M.

Both the affinity and catalytic efficiency toward GA of the PKT variant H142N identified by Yang et al.[6] were improved by substituting glutamate at position 153 with aspartate in a double mutant. However, although H142N:E153D displayed a suitably low K_M of 4 mM for biological application purposes, its maximum activity toward GA decreased by approximately 7-fold. Much of the binding energy gained in stabilizing the substrate ground state would not appear to be available for reaction TS stabilization. We are currently seeking to further stabilize TS binding in this mutant through the engineering of additional differentially oriented induced dipoles at distances further removed from the catalytic center.

The feasibility of cell-free ATP regeneration from GA with a stoichiometry of 1 mol of ATP per mol of C_2 aldehyde was demonstrated using the PKT single mutant H142N together with acetate kinase and glycerol kinase for the production of G3P. The PKT double mutant H142N:E153D did not outperform the single variant in terms of ATP regeneration from an initial GA concentration of 25 mM, likely due to its significantly lower turnover number and reduced stability under synthesis conditions. Although we are unaware of any literature reports of the glycation of asparagine or glutamine protein residues, it is feasible that the double mutant asparagine 142 side-chain carboxamide function might undergo condensation with the GA dimer to form an Amadori-rearranged 2-oxoethyl derivative.[84] Initial modeling suggests that the reactive 2-oxoethyl moiety is suitably positioned to covalently link directly to the TPP cofactor, leading to potentially structurally disruptive site-directed enzyme inactivation. In addition, the presence of an acidic residue at the neighboring residue position 153 may modulate the Amadori rearrangement rate as has been observed for other non-enzymatic protein glycation reaction mechanisms.[28,29]

In summary, our results indicate that the H142N single variant is better suited for cell-free reaction systems, whereas the H142N:E153D double mutant with its 10-fold lower K_M for GA may serve as a useful template for future engineering efforts aimed at the identification of low K_M PKT variants with improved catalytic efficiency toward glycolaldehyde for *in vivo* applications requiring low concentrations of the toxic C_2 aldehyde (e.g., acetyl-CoA synthesis from EG[6−8]). The computational differential electrostatic screening methods developed here may facilitate the identification of additional mutations capable of improving transition-state stabilization while retaining favorable substrate affinity.

The *in vitro* synthesis of up to 1.64 mol of ATP per mol of ERU via the intermediate GA was shown using the ERU-specific Bad.F6Pkt variant H256Y:H260Y:H548Y which outperformed the wild-type enzyme and the H142N variant. This experiment laid the grounds for a strategy that aimed at rapidly

https://doi.org/10.1021/acs.jpcb.6c02050
J. Phys. Chem. B 2026, 130, 7791−7808

removing the enzyme-inactivating GA from the reaction buffer by converting it to D-threose and eventually to the PKT substrate D-erythrulose through a reaction sequence catalyzed by D-threose aldolase and D-threose isomerase. We demonstrated that the use of a D-threose aldolase and D-threose isomerase in combination with the ERU-specific PKT triple mutant H256Y:H260Y:H548Y indeed enabled rapid GA consumption and an associated increase in product yield compared to direct utilization of GA by the PKT. However, despite these positive effects, incomplete substrate conversion was observed, likely due to accumulation of the aldose intermediate D-threose, which exhibited an inactivating effect on the PKT enzyme. Nevertheless, this reaction system may hold potential for *in vivo* detoxification of GA during production of the platform chemical acetyl-CoA from EG or methanol.[8,10]

Cell-free ATP regeneration from EG was achieved by combining an EG dehydrogenase and NADH oxidase with a GA-specific PKT variant, acetate kinase, and glycerol kinase. Employing the Bad.F6Pkt variant H142N or H142N:E153D resulted in a 2-fold higher maximum productivity compared to the wild-type enzyme, emphasizing the importance of a GA-specific PKT for efficient EG-based ATP-regeneration. Due to reduced stability of the double mutant under synthesis conditions, the highest yield (0.52 ± 0.02 mol_{G3P} $mol_{glycerol}^{-1}$) was obtained with the single mutant H142N.

CONCLUSION

We present a model-guided strategy to understand and engineer mutation-dependent changes in enzyme reactivity by combining physics-based electrostatic analysis, molecular modeling, and sequence-variation analysis. Applied to phosphoketolase from *Bifidobacterium adolescentis*, this approach enabled rational redesign of the active-site electric field, promoting GA dimer ring opening and improving activity toward small nonphosphorylated substrates.

Importantly, this integrative design strategy overcame epistatic limitations and enabled the rational generation of double and triple mutants with an enhanced catalytic performance. The engineered variants were successfully applied in enzyme cascades for ATP regeneration from EG, demonstrating the control of enzyme reactivity through an electrostatic design.

Overall, this study demonstrates that catalytic field engineering is an effective strategy to expand PKT substrate diversity toward smaller, nonphosphorylated substrates. The resultant PKT variants provide improved biocatalysis in GA-dependent metabolic pathways and cell-free ATP regeneration systems based on the low-cost feedstock EG.

ASSOCIATED CONTENT

Supporting Information

The Supporting Information is available free of charge at https://pubs.acs.org/doi/10.1021/acs.jpcb.6c02050.

Supporting Information 1, Protein electrostatics calculations, MSA analysis, plasmids used, and additional results (PDF)

Supporting Information 2, Primers used in this study (XLSX)

AUTHOR INFORMATION

Corresponding Author

Thomas Walther − *Chair of Bioprocess Engineering, Institute of Natural Materials Technology, TU Dresden, 01062 Dresden, Germany;* orcid.org/0000-0001-5302-1567; Email: thomas_walther@tu-dresden.de

Authors

Franziska Kraußer − *Chair of Bioprocess Engineering, Institute of Natural Materials Technology, TU Dresden, 01062 Dresden, Germany;* orcid.org/0009-0005-1782-3139

Christopher M. Topham − *Molecular Forces Consulting, 81500 Lavaur, France;* orcid.org/0000-0002-9147-0184

Kenny Rabe − *Chair of Bioprocess Engineering, Institute of Natural Materials Technology, TU Dresden, 01062 Dresden, Germany*

Jan-Ole Kundoch − *Institute of Technical Biocatalysis, Hamburg University of Technology, 21073 Hamburg, Germany*

Daniel Ohde − *Institute of Technical Biocatalysis, Hamburg University of Technology, 21073 Hamburg, Germany*

Andreas Liese − *Institute of Technical Biocatalysis, Hamburg University of Technology, 21073 Hamburg, Germany;* orcid.org/0000-0002-4867-9935

Complete contact information is available at: https://pubs.acs.org/10.1021/acs.jpcb.6c02050

Author Contributions

CMT performed the electrostatics calculations and carried out the computational structure and sequence variation analyses. CMT, FK, and TW developed the enzyme engineering strategy. FK and KR performed molecular biology work and carried out enzymatic assays. FK performed *in vitro* product syntheses. Data curation and visualization were done by FK. FK, JOK, DO, AL, and TW designed experimental setups. FK, TW, and CMT wrote the paper, which was reviewed by JOK, DO, and AL. TW conceived the cascade and supervised the project.

Notes

The authors declare no competing financial interest.

ACKNOWLEDGMENTS

The study was funded by BMBF KMU Innovativ, No. 031B1245A, and the Deutsche Forschungsgemeinschaft (DFG, German Research Foundation), Project No. 450319558. We would like to thank our colleagues Cláudio J. R. Frazão, Lisa Rothe, and Sebastian Schulz for providing the plasmids pET28a_Ms. nox, pET28a_Go.gox0313, and pET28a_Ec.fsaA_L107Y:A129G.

REFERENCES

(1) Heath, E. C.; Hurwitz, J.; Horecker, B. L.; Ginsburg, A. Pentose Fermentation by Lactobacillus Plantarum. *J. Biol. Chem.* **1958**, *231* (2), 1009−1029.

(2) Liu, L.; Zhang, L.; Tang, W.; Gu, Y.; Hua, Q.; Yang, S.; Jiang, W.; Yang, C. Phosphoketolase Pathway for Xylose Catabolism in Clostridium Acetobutylicum Revealed by ^{13}C Metabolic Flux Analysis. *J. Bacteriol.* **2012**, *194* (19), 5413−5422.

(3) Scardovi, V.; Trovatelli, L. D. The Fructose-6—Phosphate Shunt as Peculiar Pattern of Hexose Degradation in the Genus Bifidobacterium. *Ann. Microbiol Enzymol* **1965**, *15*, 19−24.

(4) Gupta, R. S.; Nanda, A.; Khadka, B. Novel Molecular, Structural and Evolutionary Characteristics of the Phosphoketolases from Bifidobacteria and Coriobacteriales. *PLoS One* **2017**, *12* (2), e0172176.
(5) Campos-Bermudez, V. A.; Bologna, F. P.; Andreo, C. S.; Drincovich, M. F. Functional Dissection of *Escherichia Coli* Phosphotransacetylase Structural Domains and Analysis of Key Compounds Involved in Activity Regulation. *FEBS Journal* **2010**, *277* (8), 1957−1966.
(6) Yang, Y.; Liu, Y.; Zhao, H.; Liu, D.; Zhang, J.; Cheng, J.; Yang, Q.; Chu, H.; Lu, X.; Luo, M.; Sheng, X.; Zhang, Y.-H. P. J.; Jiang, H.; Ma, Y. Construction of an Artificial Phosphoketolase Pathway That Efficiently Catabolizes Multiple Carbon Sources to Acetyl-CoA. *PLoS Biol.* **2023**, *21* (9), No. e3002285.
(7) Lu, X.; Liu, Y.; Yang, Y.; Wang, S.; Wang, Q.; Wang, X.; Yan, Z.; Cheng, J.; Liu, C.; Yang, X.; Luo, H.; Yang, S.; Gou, J.; Ye, L.; Lu, L.; Zhang, Z.; Guo, Y.; Nie, Y.; Lin, J.; Li, S.; Tian, C.; Cai, T.; Zhuo, B.; Ma, H.; Wang, W.; Ma, Y.; Liu, Y.; Li, Y.; Jiang, H. Constructing a Synthetic Pathway for Acetyl-Coenzyme A from One-Carbon through Enzyme Design. *Nat. Commun.* **2019**, *10* (1378), 10.
(8) Wagner, N.; Bade, F.; Straube, E.; Rabe, K.; Frazão, C. J. R.; Walther, T. In Vivo Implementation of a Synthetic Metabolic Pathway for the Carbon-Conserving Conversion of Glycolaldehyde to Acetyl-CoA. *Front. Bioeng. Biotechnol.* **2023**, *11*, 1125544.
(9) Kraußer, F.; Rabe, K.; Topham, C. M.; Voland, J.; Lilienthal, L.; Kundoch, J.-O.; Ohde, D.; Liese, A.; Walther, T. Cell-Free Reaction System for ATP Regeneration from D -Fructose. *ACS Synth. Biol.* **2025**, *14* (4), 1250−1263.
(10) Wagner, N.; Wen, L.; Frazão, C. J. R.; Walther, T. Next-Generation Feedstocks Methanol and Ethylene Glycol and Their Potential in Industrial Biotechnology. *Biotechnology Advances* **2023**, *69*, 108276.
(11) Langer, R. S. *Enzymatic Regeneration of ATP*, Massachusetts Institute of Technology, Cambridge, Massachusetts, USA, 1974.
(12) Strafford, J.; Payongsri, P.; Hibbert, E. G.; Morris, P.; Batth, S. S.; Steadman, D.; Smith, M. E. B.; Ward, J. M.; Hailes, H. C.; Dalby, P. A. Directed Evolution to Re-Adapt a Co-Evolved Network within an Enzyme. *J. Biotechnol.* **2012**, *157* (1), 237−245.
(13) Hennefarth, M. R.; Alexandrova, A. N. Advances in Optimizing Enzyme Electrostatic Preorganization. *Curr. Opin. Struct. Biol.* **2022**, *72*, 1−8.
(14) Shaik, S.; Mandal, D.; Ramanan, R. Oriented Electric Fields as Future Smart Reagents in Chemistry. *Nat. Chem.* **2016**, *8*, 1091−1098.
(15) Vaissier, V.; Sharma, S. C.; Schaettle, K.; Zhang, T.; Head-Gordon, T. Computational Optimization of Electric Fields for Improving Catalysis of a Designed Kemp Eliminase. *ACS Catal.* **2018**, *8* (1), 219−227.
(16) Siddiqui, S. A.; Stuyver, T.; Shaik, S.; Dubey, K. D. Designed Local Electric Fields−Promising Tools for Enzyme Engineering. *JACS Au* **2023**, *3* (12), 3259−3269.
(17) Ruiz-Pernía, J. J.; Świderek, K.; Bertran, J.; Moliner, V.; Tuñón, I. Electrostatics as a Guiding Principle in Understanding and Designing Enzymes. *J. Chem. Theory Comput.* **2024**, *20* (5), 1783−1795.
(18) Eberhart, M. E.; Alexandrova, A. N.; Ajmera, P.; Bím, D.; Chaturvedi, S. S.; Vargas, S.; Wilson, T. R. Methods for Theoretical Treatment of Local Fields in Proteins and Enzymes. *Chem. Rev.* **2025**, *125* (7), 3772−3813.
(19) Shao, Q.; Hollenbeak, A. C.; Jiang, Y.; Ran, X.; Bachmann, B. O.; Yang, Z. J. SubTuner Leverages Physics-Based Modeling to Complement AI in Enzyme Engineering toward Non-Native Substrates. *Chem. Catalysis* **2025**, *5* (6), 101334.
(20) Jurich, C.; Shao, Q.; Ran, X.; Yang, Z. J. Physics-Based Modeling in the New Era of Enzyme Engineering. *Nature Computational Science* **2025**, *5*, 279−291.
(21) Dittner, M.; Hartke, B. Globally Optimal Catalytic Fields - Inverse Design of Abstract Embeddings for Maximum Reaction Rate Acceleration. *J. Chem. Theory Comput.* **2018**, *14* (7), 3547−3564.
(22) Drexler, K. E. Molecular Engineering: An Approach to the Development of General Capabilities for Molecular Manipulation. *Proc. Natl. Acad. Sci. U.S.A.* **1981**, *78* (9), 5275−5278.
(23) Pabo, C. Molecular Technology: Designing Proteins and Peptides. *Nature* **1983**, *301* (5897), 200.
(24) Beker, W.; Sokalski, W. A. Bottom-Up Nonempirical Approach To Reducing Search Space in Enzyme Design Guided by Catalytic Fields. *J. Chem. Theory Comput.* **2020**, *16* (5), 3420−3429.
(25) Mariño, L.; Maya-Aguirre, C. A.; Pauwels, K.; Vilanova, B.; Ortega-Castro, J.; Frau, J.; Donoso, J.; Adrover, M. Glycation of Lysozyme by Glycolaldehyde Provides New Mechanistic Insights in Diabetes-Related Protein Aggregation. *ACS Chem. Biol.* **2017**, *12* (4), 1152−1162.
(26) Klaus, A.; Rau, R.; Glomb, M. A. Modification and Cross-Linking of Proteins by Glycolaldehyde and Glyoxal: A Model System. *J. Agric. Food Chem.* **2018**, *66* (41), 10835−10843.
(27) Kundoch, J.-O.; Ohde, D.; Byström, E.; Liese, A. Screening Platform for Immobilized Biocatalysts Utilizing Miniature Rotating Bed Reactors. *Org. Process Res. Dev.* **2024**, *28* (12), 4264−4272.
(28) Sjoblom, N. M.; Kelsey, M. M. G.; Scheck, R. A. A Systematic Study of Selective Protein Glycation. *Angew. Chem. Int. Ed* **2018**, *57* (49), 16077−16082.
(29) Uceda, A. B.; Mariño, L.; Casasnovas, R.; Adrover, M. An Overview on Glycation: Molecular Mechanisms, Impact on Proteins, Pathogenesis, and Inhibition. *Biophys Rev.* **2024**, *16* (2), 189−218.
(30) Martin, M. S.; Jacob-Dolan, J. W.; Pham, V. T. T.; Sjoblom, N. M.; Scheck, R. A. The Chemical Language of Protein Glycation. *Nat. Chem. Biol.* **2025**, *21* (3), 324−336.
(31) Szekrenyi, A.; Soler, A.; Garrabou, X.; Guérard-Hélaine, C.; Parella, T.; Joglar, J.; Lemaire, M.; Bujons, J.; Clapés, P. Engineering the Donor Selectivity of D -Fructose-6-Phosphate Aldolase for Biocatalytic Asymmetric Cross-Aldol Additions of Glycolaldehyde. *Chem.—Eur. J.* **2014**, *20* (39), 12572−12583.
(32) Zheng, L. An Efficient One-Step Site-Directed and Site-Saturation Mutagenesis Protocol. *Nucleic Acids Res.* **2004**, *32* (14), e115−e115.
(33) Studier, F. W. Protein Production by Auto-Induction in High-Density Shaking Cultures. *Protein Expression Purif.* **2005**, *41* (1), 207−234.
(34) Daudé, D.; Topham, C. M.; Remaud-Siméon, M.; André, I. Probing Impact of Active Site Residue Mutations on Stability and Activity of *Neisseria Polysaccharea* Amylosucrase. *Protein Sci.* **2013**, *22* (12), 1754−1765.
(35) Morcos, F.; Pagnani, A.; Lunt, B.; Bertolino, A.; Marks, D. S.; Sander, C.; Zecchina, R.; Onuchic, J. N.; Hwa, T.; Weigt, M. Direct-Coupling Analysis of Residue Coevolution Captures Native Contacts across Many Protein Families. *Proc. Natl. Acad. Sci. U.S.A.* **2011**, *108* (49), No. E1293-E1301.
(36) Halabi, N.; Rivoire, O.; Leibler, S.; Ranganathan, R. Protein Sectors: Evolutionary Units of Three-Dimensional Structure. *Cell* **2009**, *138* (4), 774−786.
(37) Hornak, V.; Abel, R.; Okur, A.; Strockbine, B.; Roitberg, A.; Simmerling, C. Comparison of Multiple Amber Force Fields and Development of Improved Protein Backbone Parameters. *Proteins* **2006**, *65* (3), 712−725.
(38) Wang, J.; Wolf, R. M.; Caldwell, J. W.; Kollman, P. A.; Case, D. A. Development and Testing of a General Amber Force Field. *J. Comput. Chem.* **2004**, *25* (9), 1157−1174.
(39) Lie, M. A.; Celik, L.; Jørgensen, K. A.; Schiøtt, B. Cofactor Activation and Substrate Binding in Pyruvate Decarboxylase. Insights into the Reaction Mechanism from Molecular Dynamics Simulations. *Biochemistry* **2005**, *44* (45), 14792−14806.
(40) Bayly, C. I.; Cieplak, P.; Cornell, W.; Kollman, P. A. A Well-Behaved Electrostatic Potential Based Method Using Charge Restraints for Deriving Atomic Charges: The RESP Model. *J. Phys. Chem.* **1993**, *97* (40), 10269−10280.
(41) Barca, G. M. J.; Bertoni, C.; Carrington, L.; Datta, D.; De Silva, N.; Deustua, J. E.; Fedorov, D. G.; Gour, J. R.; Gunina, A. O.; Guidez, E.; Harville, T.; Irle, S.; Ivanic, J.; Kowalski, K.; Leang, S. S.; Li, H.; Li,

https://doi.org/10.1021/acs.jpcb.6c02050
J. Phys. Chem. B 2026, 130, 7791−7808

W.; Lutz, J. J.; Magoulas, I.; Mato, J.; Mironov, V.; Nakata, H.; Pham, B. Q.; Piecuch, P.; Poole, D.; Pruitt, S. R.; Rendell, A. P.; Roskop, L. B.; Ruedenberg, K.; Sattasathuchana, T.; Schmidt, M. W.; Shen, J.; Slipchenko, L.; Sosonkina, M.; Sundriyal, V.; Tiwari, A.; Galvez Vallejo, J. L.; Westheimer, B.; Włoch, M.; Xu, P.; Zahariev, F.; Gordon, M. S. Recent Developments in the General Atomic and Molecular Electronic Structure System. *J. Chem. Phys.* **2020**, *152* (15), 154102.

(42) Wang, L.; Li, L.; Alexov, E. P *K* a Predictions for Proteins, RNA s, and DNA s with the Gaussian Dielectric Function Using DelPhi p *K* a. *Proteins* **2015**, *83* (12), 2186−2197.

(43) Pahari, S.; Sun, L.; Basu, S.; Alexov, E. DelPhiPKa: Including Salt in the Calculations and Enabling Polar Residues to Titrate. *Proteins* **2018**, *86* (12), 1277−1283.

(44) Perrin, D. D. International Union of Pure and Applied Chemistry Commission on Electroanalytical Chemistry. *Dissociation Constants of Organic Bases in Aqueous Solution: Supplement 1972*; Butterworths: London, 1972.

(45) Reynolds, W. F.; Peat, I. R.; Freedman, M. H.; Lyerla, J. R. Determination of the Tautomeric Form of the Imidazole Ring of L-Histidine in Basic Solution by Carbon-13 Magnetic Resonance Spectroscopy. *J. Am. Chem. Soc.* **1973**, *95* (2), 328−331.

(46) Emsley, P.; Lohkamp, B.; Scott, W. G.; Cowtan, K. Features and Development of *Coot*. *Acta Crystallogr. D Biol. Crystallogr.* **2010**, *66* (4), 486−501.

(47) Bondi, A. Van Der Waals Volumes and Radii. *J. Phys. Chem.* **1964**, *68* (3), 441−451.

(48) Jurrus, E.; Engel, D.; Star, K.; Monson, K.; Brandi, J.; Felberg, L. E.; Brookes, D. H.; Wilson, L.; Chen, J.; Liles, K.; Chun, M.; Li, P.; Gohara, D. W.; Dolinsky, T.; Konecny, R.; Koes, D. R.; Nielsen, J. E.; Head-Gordon, T.; Geng, W.; Krasny, R.; Wei, G.; Holst, M. J.; McCammon, J. A.; Baker, N. A. Improvements to the APBS Biomolecular Solvation Software Suite. *Protein Sci.* **2018**, *27* (1), 112−128.

(49) Humphrey, W.; Dalke, A.; Schulten, K. VMD: Visual Molecular Dynamics. *J. Mol. Graphics* **1996**, *14* (1), 33−38.

(50) Lipmann, F.; Tuttle, L. C. A Specific Micromethod for the Determination of Acyl Phosphates. *J. Biol. Chem.* **1945**, *159*, 21−28.

(51) Racker, E. [29d] Fructose-6-Phosphate Phosphoketolase from Acetobacter Xylinum. In *Methods in Enzymology*; Elsevier, 1962; Vol. *5*, pp 276−280. DOI: 10.1016/S0076-6879(62)05219-2.

(52) Morii, K.; Hosomi, S.; Terada, T.; Mizoguchi, T. Methods for Enzymatic and Colorimetric Determinations of D-Erythrulose (D-Tetrulose). *Anal. Biochem.* **1985**, *151*, 188−191.

(53) Scheidig, A. J.; Horvath, D.; Szedlacsek, S. E. Crystal Structure of a Xylulose 5-Phosphate Phosphoketolase. Insights into the Substrate Specificity for Xylulose 5-Phosphate. *J. Struct. Biol.* **2019**, *207* (1), 85−102.

(54) Nakata, K.; Miyazaki, N.; Yamaguchi, H.; Hirose, M.; Kashiwagi, T.; Kutumbarao, N. H. V.; Miyashita, O.; Tama, F.; Miyano, H.; Mizukoshi, T.; Iwasaki, K. High-Resolution Structure of Phosphoketolase from Bifidobacterium Longum Determined by Cryo-EM Single-Particle Analysis. *J. Struct. Biol.* **2022**, *214* (2), 107842.

(55) Nakata, K.; Kashiwagi, T.; Kunishima, N.; Naitow, H.; Matsuura, Y.; Miyano, H.; Mizukoshi, T.; Tono, K.; Yabashi, M.; Nango, E.; Iwata, S. Ambient Temperature Structure of Phosphoketolase from *Bifidobacterium Longum* Determined by Serial Femtosecond X-Ray Crystallography. *Acta Crystallogr. D Struct Biol.* **2023**, *79* (4), 290−303.

(56) Topham, C. M.; Barbe, S.; André, I. An Atomistic Statistically Effective Energy Function for Computational Protein Design. *J. Chem. Theory Comput.* **2016**, *12* (8), 4146−4168.

(57) Yevenes, A.; Frey, P. A. Cloning, Expression, Purification, Cofactor Requirements, and Steady State Kinetics of Phosphoketolase-2 from Lactobacillus Plantarum. *Bioorganic Chemistry* **2008**, *36* (3), 121−127.

(58) Takahashi, K.; Tagami, U.; Shimba, N.; Kashiwagi, T.; Ishikawa, K.; Suzuki, E. Crystal Structure of *Bifidobacterium Longum* Phosphoketolase; Key Enzyme for Glucose Metabolism in *Bifidobacterium*. *FEBS Lett.* **2010**, *584* (18), 3855−3861.

(59) Suzuki, R.; Katayama, T.; Kim, B.-J.; Wakagi, T.; Shoun, H.; Ashida, H.; Yamamoto, K.; Fushinobu, S. Crystal Structures of Phosphoketolase. *J. Biol. Chem.* **2010**, *285* (44), 34279−34287.

(60) Tittmann, K. Sweet Siblings with Different Faces: The Mechanisms of FBP and F6P Aldolase, Transaldolase, Transketolase and Phosphoketolase Revisited in Light of Recent Structural Data. *Bioorganic Chemistry* **2014**, *57*, 263−280.

(61) Yaylayan, V. A.; Harty-Majors, S.; Ismail, A. A. Investigation of the Mechanism of Dissociation of Glycolaldehyde Dimer (2,5-Dihydroxy-1,4-Dioxane) by FTIR Spectroscopy. *Carbohydr. Res.* **1998**, *309* (1), 31−38.

(62) Collins, G. C. S.; George, W. O. Nuclear Magnetic Resonance Spectra of Glycolaldehyde. *J. Chem. Soc., B* **1971**, 1352−1355.

(63) Azofra, L. M.; Quesada-Moreno, M. M.; Alkorta, I.; Avilés-Moreno, J. R.; Elguero, J.; López-González, J. J. Understanding the Aldo-Enediolate Tautomerism of Glycolaldehyde in Basic Aqueous Solutions. *ChemPhysChem* **2015**, *16*, 2226−2236.

(64) Warshel, A. Electrostatic Origin of the Catalytic Power of Enzymes and the Role of Preorganized Active Sites. *J. Biol. Chem.* **1998**, *273* (42), 27035−27038.

(65) Warshel, A.; Sharma, P. K.; Kato, M.; Xiang, Y.; Liu, H.; Olsson, M. H. M. Electrostatic Basis for Enzyme Catalysis. *Chem. Rev.* **2006**, *106* (8), 3210−3235.

(66) Fried, S. D.; Boxer, S. G. Electric Fields and Enzyme Catalysis. *Annu. Rev. Biochem.* **2017**, *86*, 387−415.

(67) Fersht, A. R. Catalysis, Binding and Enzyme-Substrate Complementarity. *Proc. R. Soc. London B* **1974**, *187* (1089), 397−407.

(68) Alexov, E.; Mehler, E. L.; Baker, N.; M. Baptista, A.; Huang, Y.; Milletti, F.; Erik Nielsen, J.; Farrell, D.; Carstensen, T.; Olsson, M. H. M.; Shen, J. K.; Warwicker, J.; Williams, S.; Word, J. M. Progress in the Prediction of p K_a Values in Proteins. *Proteins* **2011**, *79* (12), 3260−3275.

(69) Gunner, M. R.; Baker, N. A. Continuum Electrostatics Approaches to Calculating pKas and Ems in Proteins. In *Methods in Enzymology*; Voth, G. A., Ed.; Academic Press, 2016; Vol. *578*, pp 1−20. DOI: 10.1016/bs.mie.2016.05.052.

(70) Zhou, H.-X.; Pang, X. Electrostatic Interactions in Protein Structure, Folding, Binding, and Condensation. *Chem. Rev.* **2018**, *118* (4), 1691−1741.

(71) Tanokura, M. 1H-NMR Study on the Tautomerism of the Imidazole Ring of Histidine Residues: I. Microscopic pK Values and Molar Ratios of Tautomers in Histidine-Containing Peptides. *Biochimica et Biophysica Acta (BBA) - Protein Structure and Molecular Enzymology* **1983**, *742* (3), 576−585.

(72) Topham, C. M.; Smith, J. C. Tri-Peptide Reference Structures for the Calculation of Relative Solvent Accessible Surface Area in Protein Amino Acid Residues. *Computational Biology and Chemistry* **2015**, *54*, 33−43.

(73) Cocinero, E. J.; Lesarri, A.; Écija, P.; Cimas, Á.; Davis, B. G.; Basterretxea, F. J.; Fernández, J. A.; Castaño, F. Free Fructose Is Conformationally Locked. *J. Am. Chem. Soc.* **2013**, *135* (7), 2845−2852.

(74) Dele-Osibanjo, T.; Li, Q.; Zhang, X.; Guo, X.; Feng, J.; Liu, J.; Sun, X.; Wang, X.; Zhou, W.; Zheng, P.; Sun, J.; Ma, Y. Growth-Coupled Evolution of Phosphoketolase to Improve l-Glutamate Production by Corynebacterium Glutamicum. *Appl. Microbiol. Biotechnol.* **2019**, *103* (20), 8413−8425.

(75) Nakajima, H.; Suzuki, K.; Imahori, K. Purification and Properties of Acetate Kinase from Bacillus Stearothermophilus. *Journal of Biochemistry* **1978**, *84* (1), 193−203.

(76) Molla, G. S.; Himmelspach, A.; Wohlgemuth, R.; Haupt, E. T. K.; Liese, A. Mechanistic and Kinetics Elucidation of Mg2+/ATP Molar Ratio Effect on Glycerol Kinase. *Molecular Catalysis* **2018**, *445*, 36−42.

(77) Leang, K.; Takada, G.; Fukai, Y.; Morimoto, K.; Granström, T. B.; Izumori, K. Novel Reactions of L-Rhamnose Isomerase from

Pseudomonas Stutzeri and Its Relation with D-Xylose Isomerase via Substrate Specificity. *Biochim. Biophys. Acta* **2004**, *1674*, 68−77.
(78) Beber, M. E.; Gollub, M. G.; Mozaffari, D.; Shebek, K. M.; Flamholz, A. I.; Milo, R.; Noor, E. eQuilibrator 3.0: A Database Solution for Thermodynamic Constant Estimation. *Nucleic Acids Res.* **2022**, *50* (D1), D603−D609.
(79) Zhang, X.; Zhang, B.; Lin, J.; Wei, D. Oxidation of Ethylene Glycol to Glycolaldehyde Using a Highly Selective Alcohol Dehydrogenase from Gluconobacter Oxydans. *Journal of Molecular Catalysis B: Enzymatic* **2015**, *112*, 69−75.
(80) Yan, M.; Yin, W.; Fang, X.; Guo, J.; Shi, H. Characteristics of a Water-Forming NADH Oxidase from *Methanobrevibacter Smithii*, an Archaeon in the Human Gut. *Bioscience Reports* **2016**, *36* (6), No. e00410.
(81) Garrabou, X.; Castillo, J. A.; Guérard-Hélaine, C.; Parella, T.; Joglar, J.; Lemaire, M.; Clapés, P. Asymmetric Self- and Cross-Aldol Reactions of Glycolaldehyde Catalyzed by D-Fructose-6-Phosphate Aldolase. *Angew. Chem., Int. Ed.* **2009**, *48* (30), 5521−5525.
(82) Frazão, C. J. R.; Wagner, N.; Rabe, K.; Walther, T. Construction of a Synthetic Metabolic Pathway for Biosynthesis of 2,4-Dihydroxybutyric Acid from Ethylene Glycol. *Nat. Commun.* **2023**, *14*, 1931.
(83) Scheffen, M.; Marchal, D. G.; Beneyton, T.; Schuller, S. K.; Klose, M.; Diehl, C.; Lehmann, J.; Pfister, P.; Carrillo, M.; He, H.; Aslan, S.; Cortina, N. S.; Claus, P.; Bollschweiler, D.; Baret, J.-C.; Schuller, J. M.; Zarzycki, J.; Bar-Even, A.; Erb, T. J. A New-to-Nature Carboxylation Module to Improve Natural and Synthetic CO2 Fixation. *Nat. Catal* **2021**, *4* (2), 105−115.
(84) Hrnciar, P.; Ueda, Y.; Huang, S.; Leet, J. E.; Bronson, J. J. Synthesis of Novel Nocathiacin-Class Antibiotics. Condensation of Glycolaldehyde with Primary Amides and Tandem Reductive Amination of Amadori-Rearranged 2-Oxoethyl Intermediates. *J. Org. Chem.* **2002**, *67* (25), 8789−8793.

https://doi.org/10.1021/acs.jpcb.6c02050
J. Phys. Chem. B 2026, 130, 7791−7808